Highlights of Joint Research

Synchrotron Radiation Laboratory

Synchrotron Radiation Laboratory (SRL) has been continuing the research and developments of the 3rd generation synchrotron light source project, Super-SOR project of the University of Tokyo, which is to be constructed in the Kashiwa campus. The accelerator group of SRL is carrying out research works of the accelerator physics and developing the accelerator-related technology, many of which will be directly applied to the new light source. The staff members in the spectroscopy group are developing new experiemtnal techniques using undulator radiation. They also maintain the branch laboratory, Tsukuba branch, at KEK-Photon Factory with an undulator called Revolver, two beamlines and three experimental stations for angle-resolved photoelectron spectroscopy (ARPES), spin- and angle-resolved photoelectron spectroscopy (SARPES) and soft X-ray emission spectroscopy (XES).

The accelerator group has made a progress in the design of the Super-SOR light source. In the lattice design of the storage ring, two kinds of optics with a large dynamic aperture were prepared. The injector including a booster synchrotron and a pre-injector linac was designed so that it could be tuned to be suitable for top-up injection as well as normal injection in the single- and multi-bunch operations of the storage ring. The designs of magnet and vacuum systems were almost completed and the other ring components were also designed and developed. A new orbit correction method, eigenvector method with constraints, that we had proposed as an orbit correction method suitable for orbit feedback systems was experimentally studied by utilizing the PF-AR ring in order to confirm its performance.

The scientific highlights achieved at the three beamlines of the Tsukuba branch laboratory, are as follows. Electronic structure of the Cu-O/Ag(110)(2×2)p2mg surface was investigated by Dr Sekiba, *et al*. at BL18A (Phys. Rev. B 67, 035411 (2003)). They have discussed a scaling law describing the Slater-Koster (SK) parameters between the oxygen and d-electron metals from angle-resolved photoemission spectra. At BL-19B, Prof. Aita's group has investigated the electronic structure of $CuIr_2S_4$ (Phys. Rev. B 68, 195124 (2003)). They have discussed the effect of the lattice distortion to the charge-ordering by means of photoemission spectra and the cluster model calculations. As the joint project with Prof. Hasegawa's group, the synchrotron radiation light illuminating scanning tunneling microscope (SR-STM) project is undergoing at BL-19A. The Si $2p$ absorption spectrum from the small area of the Si surface was obtained by a STM tip, the details of which are described in this issue.

Neutron Science Laboratory

Science 1961, the ISSP has been playing a central role in neutron scattering activities in Japan not only by performing its own research programs but also by providing a general user program for the university-owned various neutron scattering spectrometers installed at research reactors of JAERI (Tokai). By spending 5 years staring from 1988, the ISSP constructed total 8.5 highly-sophisticated spectrometers both in a reactor hall and in a guide hall of the refurbished JRR-3M reactor (20MW) with cold source. In addition, Tohoku University owns 3.5 spectrometers and Kyoto University 1; therefore, total 13 spectrometers belong to the university while JAERI owns 9. In order to fully utilize these facilities, the previous Neutron Scattering Division of ISSP at Tokyo was promoted to the present Neutron Scattering Laboratory at Tokai in 1993. Since then, close to 300 proposals are submitted for the ISSP general user program for neutron scattering research each year, and the number of visiting users under this program reaches over 7000 (person-day/year). Major research areas are solid state physics (strongly correlated electron systems, high T_c superconductors, heavy fermion systems, low dimensional magnetism, high-pressure physics etc.), fundamental physics and neutron beam optics, polymer, chemistry, biology, and materials sciences.

Triple axis spectrometers and a high resolution powder diffractometer were utilized for a conventional solid state physics and a variety of research fields on hard-condensed matter, while in the field of soft-condensed matter physics, researches were mostly carried out by using the small angle neutron scattering (SANS-U) and/or neutron spin echo (NSE) instruments. In the fiscal year of 2002, the research topics on the hard-condensed matter science covered stripe order in high-T_c superconductors, and closely related 2 dimensional systems, charge and orbital ordering in CMR

manganites, quadrapolar ordering in rare-earth based inter-metallic compounds, spin dynamics of low dimensional dimmer systems, etc. On the other hand, the research topics on the soft-condensed matter science covered structure characterization of polymer blends, micelles, amphiphilic polymers block copolymers, liquid crystals, proteins, inorganic gels, dynamics of brush-polymers on surface, slow dynamics of surfactants, pressure dependence of dynamics of amphiphilic membranes, and so on. The details of individual studies are reported in the NSL-ISSP Activity Report.

Supercomputer Center

The supercomputer system in the Supercomputer Center of the Institute (SCC-ISSP) is placed at the service of general researchers of condensed matter physics through the User Program conducted by the Materials Design and Characterization Laboratory (MDCL). One of its aims is to selectively promote and support huge computations which are hardly carried out on other computers such as work-station clusters in individual laboratories.

The SCC-ISSP main system consists of two supercomputers. Hitachi SR8000/60, called System-A, is a distributed-memory-type parallel supercomputer with 60 nodes, 640GB memory in total and 12x60GFlops peak performance. On the other hand, SGI Origin 2800/384, called System-B, is a massively parallel supercomputer with 192GB memory in total and 0.8x384GFlops peak performance.

A project(s) can be proposed by any staff in universities or public research institutes in Japan. The projects proposed are judged by the Steering Committee of the SCC-ISSP, under which the Supercomputer Project Advisory Committee is formed to review proposals. In fiscal year 2003 totally 143 projects were approved. The total points applied and approved are listed on Table. 1 below.

The research projects are roughly classified into the following three (the number of projects approved):

First-Principles Calculation of Materials Properties (50)
Strongly Correlated Quantum Systems (62)
Cooperative Phenomena in Complex, Macroscopic Systems (31)

All the three involve both methodology of computation and its applications. The results of the projects are reported in 'Activity Report 2003' of the SCC-ISSP. In the report the following four invited articles are included in this year:

"First-Principles Study on N/Cu(001)" by Y. Yoshimoto and S. Tsuneyuki,
"Ab-Initio Quantum Dynamics Calculation of Hydrogen Interaction with Surfaces ---Exploiting the Inherent Orientation Dependence of Hydrogen-Surface Reactions---" by W. A. Diño and H. Kasai,
"Mott Transition in Multi-Orbital Electron Systems" by N. Kawakami,
"Randomness Effects on Quantum Phase Transitions of Bond-Alternating Haldane Chain" by S. Todo, T. Arakawa and H. Takayama.

For communicating information not only on the SCC-ISSP but on general research activities in the field of `Computational Material Physics', the home page
    http://www.issp.u-tokyo.ac.jp/public/cmp
and the mailing list `cmp-ml' are open to community of the field.

Table 1: Research projects approved in 2003

| Class | Max.Point | Application | # of Proj. | Total points Applied | | Approved | |
				Sys-A	Sys-B	Sys-A	Sys-B
A	100k	any time	4	210K	190K	210K	190K
B	2M	twice a year	44	58.7M	23.55M	58.5M	23.55M
C	20M	twice a year	90	996.9M	508.6M	815.2M	481.0M
D	none	any time	5	150.0M	70.0M	71.0M	70.0M

For System-A 1 K point corresponds to charge for CPU time of about 0.43 hours by one processing element, while the corresponding figure is 2.32 hours for System-B. For one of the D class projects, a special queue which exclusively uses 2 nodes of system-A was allowed to perform extremely long-time jobs necessary.

Anomalous Behaviour Close to the Metamagnetic Quantum Critical Point in Sr$_3$Ru$_2$O$_7$

R.S. Perry, Y. Maeno, and T. Sakakibara

Quantum criticality continues to generate much interest within the international condensed matter community. Conventional phase transitions occur when a system changes state, for example as the temperature of water is lowered it freezes to create ice. However, it is also possible to change the state of a system using a non-thermal variable, for example pressure, magnetic field or chemical concentration. When such a phase transition occurs at zero temperature then quantum fluctuations, as opposed to thermal or classical fluctuations, dominate the properties of the material. In this region of the phase diagram novel behaviour, for example unconventional superconductivity [1], has been observed.

Up to now, both pressure and chemical concentration have almost exclusively been used to tune materials to quantum criticality. Recently magnetic-field-induced (MFI) quantum phase transitions have become the subject of attention due to the ease with which they can be accessed experimentally and the opportunity to study the critical behaviour low disorder environments. A relatively unusual MFI phase transition occurs in metallic metamagnetic systems. These are materials close to a ferromagnetic instability that undergo a MFI first order phase transition into a higher polarized state at a critical field B_M. The phase diagram naturally involves a classical critical point terminating a line of first order phase transitions, and quantum critical behaviour can occur if the critical point sits at zero temperature. This may seem to be a fairly unlikely scenario, but just such a situation is realized in the bilayered perovskite ruthenate Sr$_3$Ru$_2$O$_7$ [2].

Sr$_3$Ru$_2$O$_7$ is a strongly correlated (electronic specific heat, γ = 110 mJ/Ru mol K^2), d band (4d^4), Fermi liquid metal exhibiting a metamagnetic transition with B_M=7.9 T (for the field perpendicular to the ruthenium oxygen planes). Previously, it was shown that the Fermi liquid state is suppressed as a function of magnetic field and non-Fermi liquid behaviour extending to high temperatures was measured in the vicinity of the quantum critical point (see figure 1) [2].
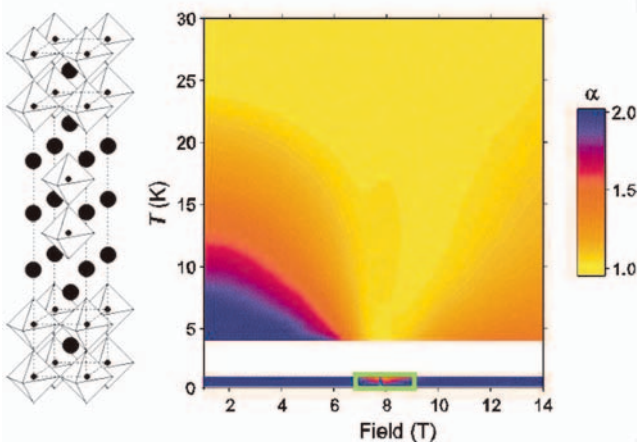

Fig. 1. (left) The bilayered perovskite structure of Sr$_3$Ru$_2$O$_7$. The large solid circles are Strontium atoms and the small solid circles are Ruthenium atoms surrounded by oxygen atoms. (right) Plot of the resistivity ρ temperature exponent α (defined as $\rho = \rho_{res} + A.T^\alpha$) as a function of field and temperature. α =2 (blue) implies a Fermi liquid power law. The system can be tuned from Fermi liquid at low and high fields to non-Fermi liquid close to the critical field (7.9 T).
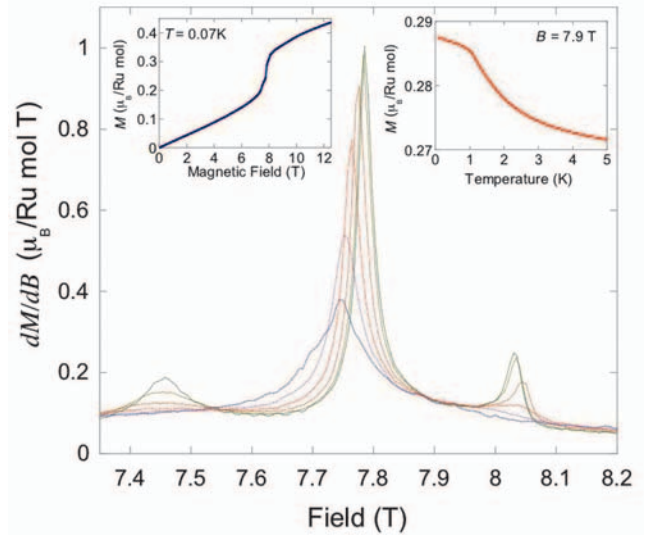

Fig. 2. Recent low temperature magnetization measurements made on ultra pure single crystals of Sr$_3$Ru$_2$O$_7$. (main plot) The static susceptibility at 0.91 K, 0.74 K, 0.54 K, 0.36 K, 0.18 K and 0.07 K (from blue to green). Three metamagnetic transitions are clearly resolved. (left inset) The magnetization versus magnetic field at 70 mK. (right inset) The magnetization as a function of temperature inside the critical region (7.9 T).

In ultra clean samples (impurity resistivity ~ 0.5 $\mu\Omega$cm) even more anomalous behaviour in the resistivity at low temperatures has been observed around B_M [3]. In order to probe the thermodynamic properties of the system we have made the first low temperature magnetization measurements on ultra clean samples [4]. The samples were grown by floating zone technique at Kyoto University.

The metamagnetic signature, i.e. the step in the magnetization, is clearly observed as shown in the left inset in Fig. 2. Within an itinerant model, this step originates from a change in the topography of the spin polarized Fermi surfaces. As such, the critical fluctuations can be considered to be fluctuations of the Fermi surface itself. Around B_M multiple metamagnetic transitions have been resolved (see main plot in Fig. 2). The transitions at 7.8 T and 8.0 T are first order (from dynamic susceptibility measurements) and coincide with the anomalous peak in the magnetoresitivity [3]. The observation of multiple metamagnetic transitions in an itinerant system is fairly unique in itself but what is particularly interesting is the temperature dependence of the peaks at 7.8 T and 8.0 T. $\partial T_{peak}/\partial B_M$ <0 and >0 for the 7.8 T and 8.0 T transitions, respectively. Within a mean field theory of itinerant electron magnetism involving, for example, proximity of the Fermi surface to multiple peaks in the density of states, B_M would be expected to increase with temperature. More intriguing still is the temperature dependence of the magnetization for magnetic fields between 7.8 T and 8.0 T (see right inset to Fig. 2). Far for B_M, Pauli behaviour was observed. At B_M = 7.9 T, the magnetization increases smoothly as a function of temperature, as one would expect for the approach to a critical point. However, at ~1 K a distinct change of slope is observed. This feature coincides with a minimum observed in the resistivity as a function of temperature. It should be noted that this anomalous, non-Fermi liquid behaviour is only observed between these two first order phase transitions.

The work so far raises several interesting questions. Why does the behaviour of the magnetization deviate from mean field theory? Is this a consequence of proximity to a quantum critical point? What causes the cut-off in the

divergence of the fluctuations very close to B_M and for temperatures less than 1 K? We are currently working on resolving these issues and are planning measurements, including uniaxial pressure work, in the future.

References
[1] N. D. Mathur *et al.*, Nature **394**, 6688 (1998).
[2] S. A. Grigera *et al.*, Science **294**, 5541 (2001).
[3] R. S. Perry *et al.*, Phys. Rev. Lett. **92**, 166602 (2004).
[4] R. S. Perry, T. Tayama, T. Sakakibara and Y. Maeno, in preparation.

Authors
R. S. Perry[a,b], T. Tayama, K. Kitagawa[a], T. Sakakibara, K. Ishida[b], and Y. Maeno[a,b]
[a] Department of Physics, Kyoto University.
[b] Kyoto University International Innovation Center

Electron Correlation and Molecular Vibration in the Strongly Correlated Organic Conductors

T. Sasaki and H. Tajima

A series of the κ-type BEDT-TTF organic superconductors has attracted considerable attention from the point of view of the strongly correlated Q2D electron system. The unconventional metallic, antiferromagnetic insulator and superconducting phases appear next to one another in the phase diagram. The transitions among these phases are controlled by the applied pressure, which must change the conduction bandwidth W with respect to the effective Coulomb repulsion U on a dimer. Optical conductivity measurements are powerful tool for investigating such correlated electron system. We focus on the change of a specific molecular vibration mode $v_3(a_g)$ of κ-(BEDT-TTF)$_2$Cu[N(CN)$_2$]X (X=Br and Cl). The symmetric $v_3(a_g)$ mode becomes visible in the IR spectra due to the large electron-molecular vibration (EMV) coupling. Thus the mode is sensitive to the electronic state on the BEDT-TTF dimer.

Figure 1 shows the optical conductivity of X=Br and Cl salts. The peaks at 1320-1330 for $E//c$ and 1250-1270 cm^{-1} for $E//a$ shift to higher frequency below about 30-40 K in X=Br, and to lower frequency below 50-60K in X=Cl . The former temperature corresponds to T^* and the latter T_{ins}. These relatively broad peaks have been assigned to the $v_3(a_g)$ mode. In concurrence with such frequency shifts, the shape of the conductivity peaks change at T^* and T_{ins}. The peak becomes sharper and larger below T_{ins} in X=Cl, while the further broadening seems to be observed below T^* in X=Br.

The peak frequency ω_{IR} of the $v_3(a_g)$ mode is shown in the inset of Figure 2. The peak frequencies in both salts and both polarization directions increase monotonically with decreasing temperature from room temperature. This monotonic change of ω_{IR} is in accordance with the change of the same mode of the Raman shift frequency ω_R. Then the monotonic change of ω_{IR} and ω_R represents the hardening of the molecular viblation itself by cooling. Below about T_{ins} =50-60K, however, the peak frequency starts to shift to lower frequency in both polarization directions of X=Cl. Then a small downward jump appears at T_N = 28K. To the contrary, the same $v_3(a_g)$ mode of superconducting X=Br shifts to the higher frequency abruptly below T^* = 38 K in both the polarization directions. The characteristic temperature dependence of the $v_3(a_g)$ mode in the IR optical conduc-
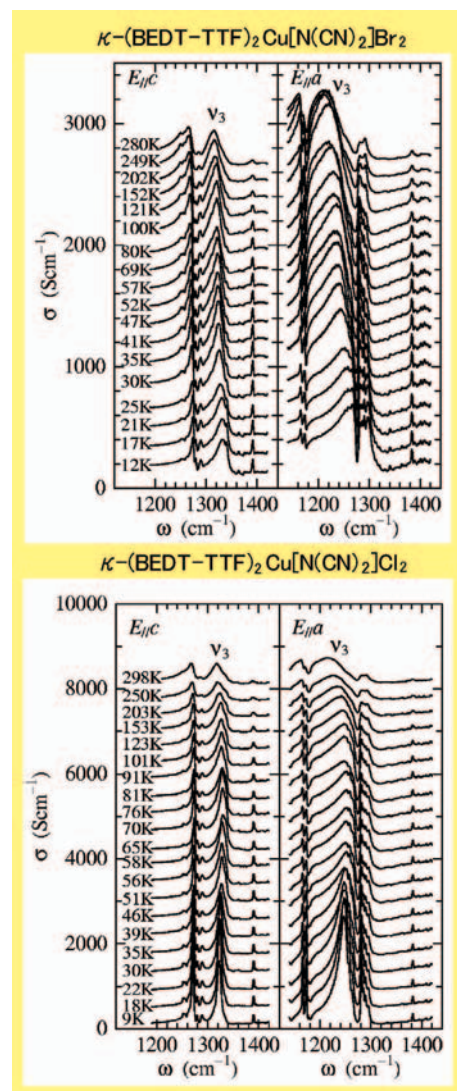

Fig. 1. The conductivity spectra of κ-(BEDT-TTF)$_2$Cu[N(CN)$_2$]Br and κ-(BEDT-TTF)$_2$Cu[N(CN)$_2$]Cl. The peaks at 1320-1330 for $E//c$ and 1250-1270 cm^{-1} for $E//a$ are assigned to the EMV coupled $v_3(a_g)$ mode.
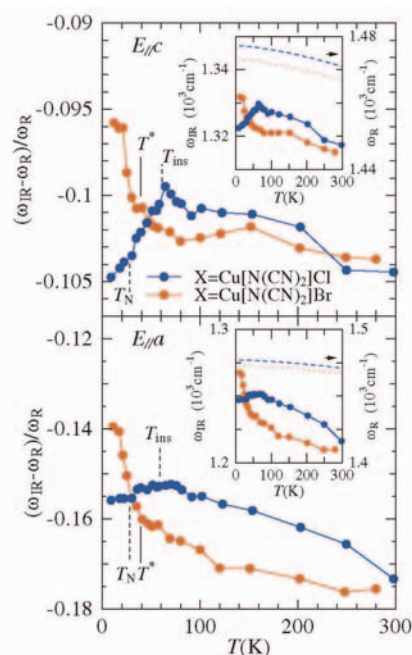

Fig. 2. Temperature dependence of the IR conductivity peak frequency (ω_{IR}) of the $v_3(a_g)$ mode normalized by the same mode of the Raman shift (ω_R) in κ-(BEDT-TTF)$_2$Cu[N(CN)$_2$]Br and κ-(BEDT-TTF)$_2$Cu[N(CN)$_2$]Cl. Insets show the temperature dependence of ω_{IR} and ω_R.

tivity can be attributed to the change of the electronic states through the EMV coupling. The main panel of Fig. 2 shows the temperature dependence of the relative frequency shift of the $\nu_3(a_g)$ mode in the IR spectra, which is normalized by ω_R shown in the inset.

The IR frequency ω_{IR} is expected to be smaller than the bare phonon frequency ω_0 ($\approx \omega_R$) when the transfer integral t_{dimer} for hopping between molecules within the dimer is larger than ω_0 ($\approx \omega_R$). These plots support further that the anomalous frequency shifts of the $\nu_3(a_g)$ mode at T^* in X=Br, and T_{ins} in X=Cl are caused by changing not the molecular vibration itself but the electronic states on the dimers through the EMV coupling.

In view of such change of ω_{IR} of the $\nu_3(a_g)$ mode, let us then consider the relation to the electronic states. In the κ-type BEDT-TTF system, the effective half filling bands are expected and results in the Mott insulator due to the strong dimerization. This situation is realized below T_{ins} in X=Cl. Large negative frequency shift from the bare phonon frequency observed below T_{ins} corresponds to the enhancement of the EMV coupling. The large EMV coupling on the dimer system implies that the carriers tend to localize at the dimer and then the conductivity becomes small. The larger and sharper peak shape of the $\nu_3(a_g)$ mode also demonstrates the localization of a carrier (one hole) at each dimer. Then the system has became the Mott insulating state before the AF static order appears at T_N. On the other hand, the positive frequency shift below T^* indicates that the carriers on the dimer show the itinerant behaviour in the superconducting salt.

Reference

[1] T. Sasaki *et al.*: Phys. Rev. B **69**, 064508 (2004).

Authors
T. Sasaki[a], I. Ito[a], N. Yoneyama[a], N. Kobayashi[a], N. Hanasaki, H. Tajima, T. Ito[b], and Y. Iwasa[a].
[a]Institute for Materials Research, Tohoku University
[b]JAIST Hokuriku

Biferrocenium Charge-Transfer Salts with M(mnt)₂. Successive Valence Transitions Coupling with 1-D Magnetic Instability of the Anion

T. Mochida and H. Mori

Electron transfer phenomena in biological systems as well as in molecular materials have attracted considerable attention for years. We have focused on the electron transfer processes in biferrocenium salts as an approach to novel electronic functions [1, 2]. To introduce conducting and/or magnetic functions into biferrocenium charge-transfer complexes, we chose M(mnt)₂ (mnt = maleonitrilodithionate) as the counter anion, and prepared (1',1'''-R₂-1,1''-biferrocene)[M(mnt)₂] (**1a**: R = isopropyl; **2a**: R = dineopentyl) and (1',1'''-R₂-1,1''-biferrocene)₂[Co(mnt)₂]₂ (**1b**: R = isopropyl; **2b**: R = dineopentyl). Complexes **1a** and **1b** showed segregated-stack crystal structures, while molecular arrangements in **2a** and **2b** were discrete. All the complexes contain mixed-valent biferrocenium monocations.

Here we focus on the unusual successive valence transitions found in the crystal of **1a**. The ^{57}Fe Mössbauer spectra indicates the presence of valence ordering processes of the cations at around 250 K and 120 K (Fig. 1). The origin for

the phenomenon has been elucidated by means of low-temperature X-ray crystallography and calorimetry; the unit cell at room temperature contains two crystallographically independent biferrocenium cations, one of which undergoes valence localization at around room temperature, whereas the other one below 120 K. The former transition is a thermal process, which originates from an asymmetrical effect of the crystal environment around the cation, while the latter
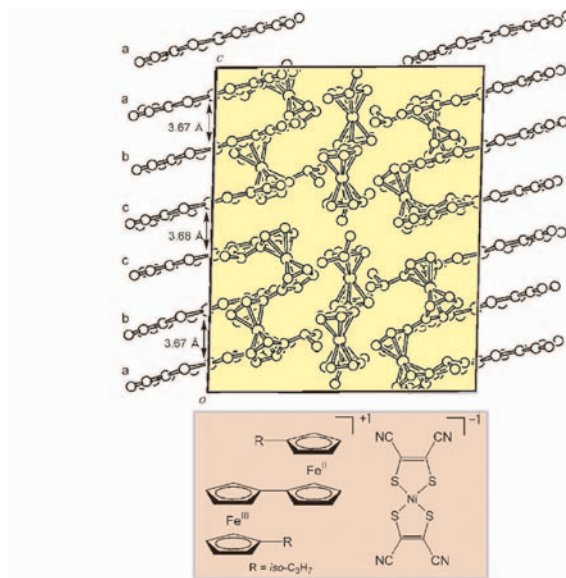

Fig. 1. Packing diagram of (1',1'''-isopropyl-1,1''-biferrocene) [Ni(mnt)₂] in the low-temperature phase (90 K), together with the structural formula. The acceptors constitute a uniform column at room temperature, while dimerization occurs in the low temperature phase, as seen in the Figure.
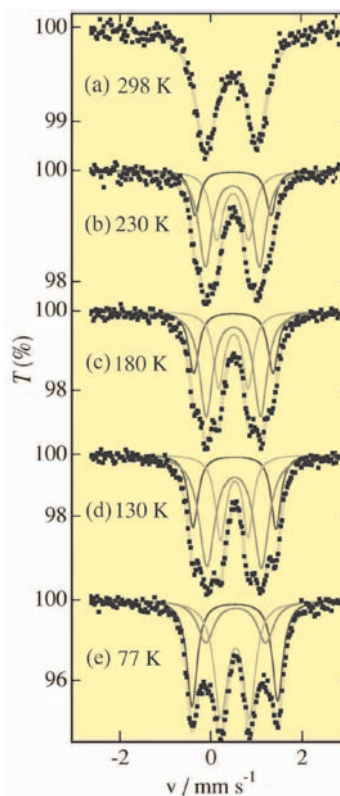

Fig. 2. ^{57}Fe Mössbauer spectra of complex **1a**, suggesting the presence of successive valence transitions. A doublet signal is seen above 298 K, which is characteristic of a valence-detrapped state of the cation. Below 230K, the spectra show three doublets, which indicates the coexistence of valence-detrapped and valence-trapped species. At temperatures below 100 K, the spectra show two doublets, being characteristic of a valence-trapped state.

transition is coupled with a phase transition that accompanies a cell-doubling. The transition is associated with a spin-Peierls-like dimerization of the acceptor (Fig. 2), which is also manifested in its temperature dependent magnetic susceptibility. Thus, the 1-D instability of the $Ni(mnt)_2$ spins was found to trigger the charge localization of the cation through symmetry-lowering of the crystal environment. On the other hand, complexes **1b**, **2a**, and **2b** exhibited trapped-valence states at room temperature. The strong tendency of charge localization in these salts was shown to originate from local electrostatic interactions.

References
[1] T. Mochida, S. Yamazaki, S. Suzuki, S. Shimizu, and H. Mori, Bull. Chem. Soc. Jpn., **76**, 2321-2328 (2003).
[2] T. Mochida, Mol. Cryst. Liq. Cryst., **343**, 205 (2000).

Authors
T. Mochida[a], K. Takazawa[a], H. Matsui[a], M. Takahashi[a], M. Takeda[a], M. Sato[a], Y. Nishio[a], K. Kajita[a], and H. Mori
[a]Toho University

New Mixed Valence Cobalt Oxides, $ABaCo_4O_7$ (A: Ca, Dy-Lu)

N. Nakayama and Y. Ueda

The mixed valence cobalt oxides, such as Na_xCoO_2 or $YBaCo_2O_{5+x}$, are known to show interesting magnetic and electrical properties. We have synthesized new mixed valence cobalt oxides $ABaCo_4O_7$ (A: Ca, Dy-Lu) iso-structural to $YBaCo_4O_7$ recently reported. Ba and O atoms form a close packed structure with 4H (*abac*) stacking, in which A and Co atoms occupy the octahedral and tetrahedral sites, respectively. The CoO_4 tetrahedra form a non-centrosymmetric lattice ($P6_3mn$) by the corner sharing, where the Co kagomé lattice and the ordered ACo triangular lattice are stacked alternately. The Lu and Ca compounds are particularly interesting because A-site atoms are nonmagnetic. The formula valences of Co in $LuBaCo_4O_7$ and $CaBaCo_4O_7$ are 2.25 and 2.5, respectively. The crystal symmetry of $CaBaCo_4O_7$ is lowered to orthorhombic $Cmc2_1$, suggesting the charge ordered state of Co(II) and Co(III). No evidence of the charge ordering for $LuBaCo_4O_7$ was detected at room temperature. However, $LuBaCo_4O_7$ shows a phase transition indicating the charge ordering at low temperature.

$LuBaCo_4O_7$ shows an antiferromagnetic ordering below 50 K, whereas $CaBaCo_4O_7$ shows a ferromagnetic ordering below 60 K. The fundamental magnetic interaction in the Co lattice is antiferromagnetic. Above the magnetic ordering
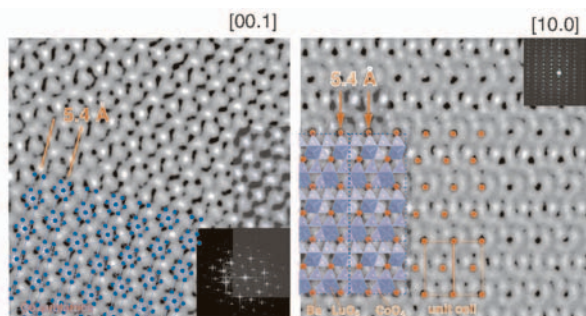

Fig. 1. High resolution lattice images of $LuBaCo_4O_7$ (a=6.264 Å, c=10.227 Å; $P6_3mc$, Z=2). The non-centrosymmetric structure is clearly resolved when viewed along [10.0].
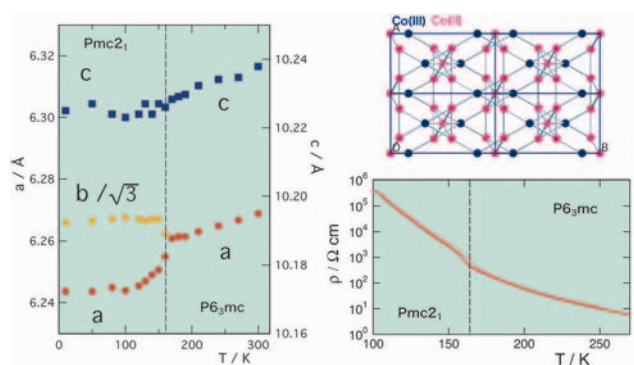

Fig. 2. The temperature dependence of lattice parameters and the electrical resistivity for $LuBaCo_4O_7$. The phase transition at 160 K must be originated from the charge ordering in the Co sublattice. A tentative ordered structure of Co(II) and Co(III) in the low temperature orthorhombic $Pmc2_1$ phase is also shown.

temperature, $LuBaCo_4O_7$ shows a first order phase transition at around 160 K, which can be clearly detected by electrical resistivity, heat capacity, x-ray diffraction and electron diffraction. X-ray and electron diffraction patterns indicate that the crystal symmetry lowers to orthorhombic $Pmc2_1$. The increase of the electrical resistivity in the low temperature phase also suggests that the phase transition is originated from the charge ordering. The magnetic susceptibility also shows a small decrease of paramagnetic effective moments (from 1.75 to 0.99 μ_B) below 160 K indicating a change in the spin state. Similar phase transitions were observed for $YbBaCo_4O_7$ and $TmBaCo_4O_7$ at 175 K and 230 K, respectively. The investigations on the charge ordered structures and the oxygen non-stoichiometry are now in progress.

Authors
N. Nakayama[a], T. Mizota[a], A. N. Vasil'ev[b], M. Isobe, and Y. Ueda
[a] Faculty of Engineering, Yamaguchi University
[b] Low Temperature Physics and Superconductivity Department, Moscow State University

Quantum-Number Projected Path-Integral Renormalization Group Method

M. Imada

Symmetry plays a crucial role in understanding quantum many-body systems. For example, the Hubbard model preserves total spin, total momentum, and some geometrical symmetries on a lattice, by which we can classify low-energy eigenstates and can elucidate the nature of low-energy phenomena like excitation spectra and spectroscopic properties.

For strongly correlated electron systems, numerical approaches are an indispensable tool for their studies and various methods such as quantum Monte Carlo methods and Density Matrix Renormalization Group method have been presented, while except exact diagonalization method whose tractable system size is severely limited, these methods cannot fully take an advantage of symmetry and excitation spectra have not been well explored.

Recently we have developed a quantum-number projection technique [1], by which advantage of symmetry can be fully extracted. For instance, we can handle wave functions with definite and exact symmetries and lowest energy state
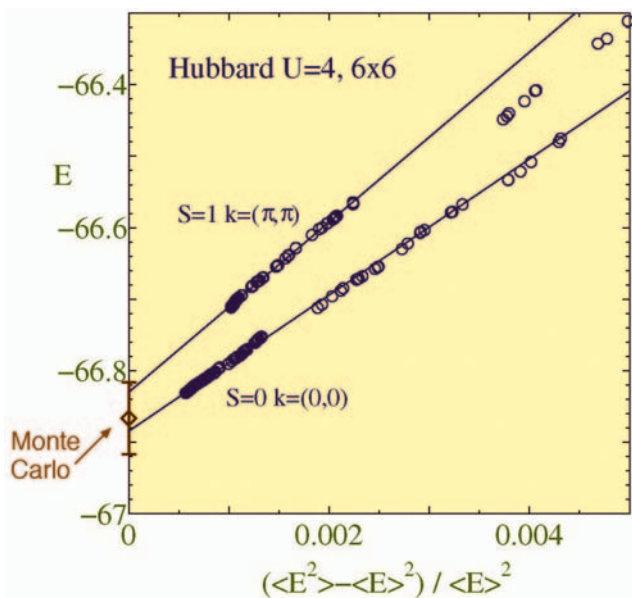
Fig. 1. We demonstrate the efficiency of the QP-PIRG [1] in the case of the 2D half-filled Hubbard model with 6 by 6 square lattice and the periodic boundary condition. The parameters are at t=1, t'=0 and U=4. The energy is obtained by the extrapolation of the energy to the zero energy variance [2]. The extrapolations of the ground state (S=0, k=(0,0)) and first excited state (S=1,k=(π,π)) energies are shown. Although exact ground state energy is not available, the ground-state energy of Monte Carlo calculation is shown by open diamond at zero variance with its statistical error bar. The ground state energy by the QP-PIRG is within the error-bar of the Monte Carlo calculation.

with different symmetries can be treated in the same footing of ground state. Moreover we have presented its implementation [1] to the path-integral renormalization group (PIRG) method [2] and succeeded in extremely enlarging the feasibility of the PIRG.

The quantum-number projection method can pick up a component with required symmetries from symmetry broken wave functions. In the Hubbard-type models, symmetries such as spin and momentum have a significant role in the low-energy states, while explicit construction of symmetry imposed wave function is quite complicated for a large number of electrons. However, the quantum-number projection technique enables us to easily handle symmetry-imposed wave function in a compact and numerically tractable form by integral or summation [1]. For instance, for spin symmetry, we can consider spin projection, which is represented by one-dimensional integral over Euler's angle in spin space. The present spin projection is a counterpart of angular momentum projection, which is often used in nuclear many-body problem. The momentum projection is also simply given from the superposition of spatially translated basis functions. Geometrical symmetry on a lattice such as the inversion and rotation symmetries is also considered in the similar way. By this method we can exactly treat spin, momentum and other quantum numbers to investigate the Hubbard-type models.

Moreover this method is well harmonized with the PIRG [2]. In this method, the wave function is expressed by a linear combination of L basis states which are deliberately optimized by the auxiliary-field Quantum Monte Carlo technique [2], while the symmetries are not retained in each basis state in general because the numerically manageable number of the basis states, L, is limited. Therefore by applying the quantum-number projection onto each basis state, we can implement it into the PIRG. Consequently we can exactly treat the symmetry and extract the state with specified

quantum numbers by the PIRG. Concerning its procedure for quantum-number projection and PIRG process, we have proposed two ways of implementing quantum-number projection into the PIRG [1]. One way is to carry out quantum-number projection afterwards for the already obtained PIRG wave function (PIRG+QP). Other is to carry out the PIRG by using quantum-number projected basis states (QP-PIRG). By both methods, the ground state can be efficiently extracted by specifying the quantum number with higher accuracy than the PIRG without projection. Comparing these two methods, the latter method can give more accurate eigenenergy than the former does.

By this extension of the PIRG, we have made following essential progresses: (1) Precision of the numerical calculation is substantially improved. (2) The quantum number of the ground state is exactly determined. (3) The extended PIRG by the quantum-number projection can handle excited states and their spectroscopic properties in addition to the ground state.

As a numerical demonstration, we investigate the standard Hubbard model on two-dimensional square lattice. We can obtain an excited state with S=1 and k=(π, π) in addition to the ground state with S=0 and k=(0,0) for the 6x6 half-filled lattice with U/t=4 as shown in Fig. 1. The ground state energy by the QP-PIRG is very close to one by the Monte Carlo method and the QP-PIRG can obtain the excited energy in addition to the ground state energy. We also test the QP-PIRG in the case of t-t' Hubbard model with large geometrical frustration effect and with severe minus sign problems in term of Monte Carlo methods. We consider the half-filled system on 4 by 4 lattice with U/t=5.7 and t'=0.5 and confirmed that the total energy difference between the present result and exact one is very small and is less than 0.01 [1].

Recently by using the PIRG method, the non-magnetic insulator (NMI) phase has been found near the Mott transition for relatively large t' [4]. As the present extended PIRG can explicitly handle quantum numbers, it will be useful to clarify its nature. It is also worth noting that the present quantum-number projection technique and the PIRG method work well irrespective of the details of the considered system. Therefore the present approach will work for other systems in addition to Hubbard-type models.

References
[1] T. Mizusaki and M.Imada, Phys. Rev. B**69**, 125110 (2004).
[2] M. Imada and T. Kashima, J. Phys. Soc. Jpn. **69**, 2723 (2000); T. Kashima and M. Imada, J. Phys. Soc. Jpn. **70**, 2287 (2001).
[3] M. Imada, T. Mizusaki, S. Watanabe, cond-mat/0307022.
[4] T. Kashima and M. Imada, J. Phys. Soc. Jpn., **70**, 3052 (2001); H. Morita, S. Watanabe and M. Imada, J. Phys. Soc. Jpn., **71**, 2109 (2002),
[5] Y. Noda and M. Imada, Phys. Rev. Lett., 89, 176803 (2002).

Authors
T. Mizusaki[a] and M. Imada
[a] Institute of Natural Sciences, Senshu University

"Half Metallicity" of a Diluted Magnetic Semiconductor (Ga, Mn)As

E. Kojima, S. Katsumoto, and M. Kuwata-Gonokami

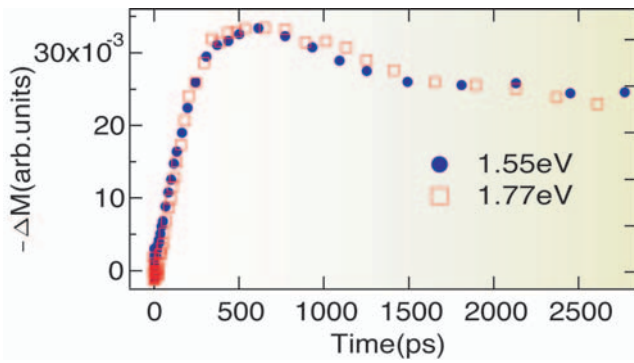Since the first synthesis of a III-V based diluted magnet-

Fig. 1. Temporal evolution of the extracted magnetization component. The data are normalized at the maximum point. A positive direction shows demagnetization. A solid line shows a result obtained using the three temperature model considering thermal diffusion.

ic semiconductor (Ga,Mn)As [1], it has attracted attentions due to its high (110K) Curie temperature, high controllability in structure and good connectivity to sophisticated GaAs-based superstructures. The origin of the ferromagnetism in such a diluted spin system has been the most important problem in this system from both the physics and the applications because the Curie temperature is still not high enough to be applied to so called spintronics devices, working at room temperatures. There have appeared many theoretical proposals and interestingly many of them predicts half-metallic band structure [2], *i.e.*, at the Fermi surface only single spin subband exists and hence spin injection with the efficiency of 100% is, in principle, possible [3]. Though no sound experimental evidence has been given to this attractive hypothesis.

In order to investigate this problem we performed time-resolved magneto-optical Kerr effect (TR-MOKE) measurement [4,5], in which the spin and carrier dynamics can be simultaneously probed. The "three temperature modeling" of the transient properties of reflectivity etc. can lead to the observation of spin-charge thermal isolation, which is strong evidence of the half metallicity.

Though TR-MOKE is a powerful technique, always a problem is the extraction of the pure magnetization component from the MOKE signal. In order to overcome the difficulty, we developed a two-color probe method, with which time-dependent magnetization after an initial strong excitation is successfully extracted as shown in Fig.1.

In Fig.1, after rapid change in the magnetization, very slow relaxation is observed. Such very slow oscillation can only be explained by assuming that the density of states for one spin direction is much smaller than that of the other direction, *i.e.*, this observation constitutes direct evidence of half metallicity in (Ga,Mn)As.

References
[1] H. Ohno, A. Shen, F. Matsukura, A. Oiwa, A. Endo, S. Katsumoto, and Y. Iye, Appl. Phys. Lett. **69**, 363 (1996).
[2] *e. g.*, H. Akai, Phys. Rev. Lett. **81**, 3002 (1998).
[3] M. Tanaka and Y. Higo, Phys. Rev. Lett. **87**, 026602 (2001).
[4] T. Kise, T. Ogasawara, M. Ashida, Y. Tomioka, Y. Tokura and M. Kuwata-Gonokami, Phys. Rev. Lett. **85**, 1986 (2000).
[5] E. Kojima, R. Shimano, Y. Hashimoto, S. Katsumoto and M. Kuwata-Gonokami, Phys. Rev. B **68**, 193203 (2003).

Authors
E. Kojima, S. Katsumoto, and M. Kuwata-Gonokami[a]
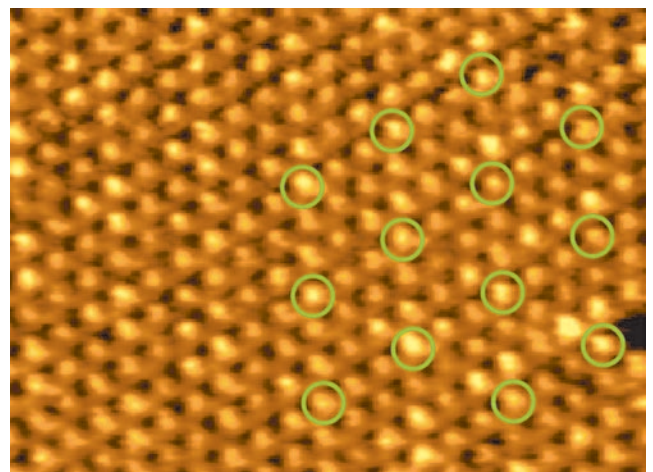[a]Department of Applied Physics, The University of Tokyo

Development of Milli-Kelvin Scanning Tunneling Microscope

Y. Hasegawa M. Kubota, and A. Sakai

An ultralow temperature scanning tunneling microscope (STM) was developed by installing an STM head in a dilution refrigerator. Atomic images and tunneling spectra showing a superconducting gap were taken on a cleaved surface of $2H$-$NbSe_2$ with the sample cooled down to 90mK.

The STM was constructed by attaching a home-made STM head on a mixing chamber of a commercial dilution refrigerator. The head is compact with ca. 30 x 30 x 50 mm^3 in size, so that it can be fitted into an internal vacuum chamber (IVC) containing cooled parts of the refrigerator. A linear motion motor developed by Pan *et al*. is used for coarse approaching. A sample holder can be transferred between the STM head and a UHV preparation chamber where one can do basic surface preparation of samples, such as annealing, deposition and so on.

In order to test its performance, we carried out STM and tunneling spectroscopic studies on a cleaved surface of $2H$-$NbSe_2$. The sample shows charge-density-wave (CDW) and superconducting transitions at 33 K and 7.2 K, respectively.

Figure 1 shows an STM image taken at the sample tem-

Fig. 1. STM image of the cleaved surface of $2H$-$NbSe_2$ taken at a sample temperature of 90 mK. The size of the observed area is 4.6 nm $\times$ 6.2 nm.
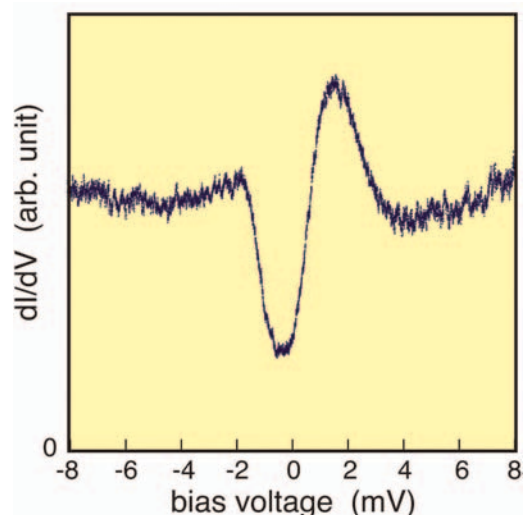

Fig. 2. dI/dV spectrum taken on the $NbSe_2$ surface at 90 mK.

perature of 90 mK. Atomic arrangement of the surface with a unit distance of 0.35 nm can be clearly observed. A slight modulation in height with a periodicity of 3 times unit cell, marked with green circles in Fig. 1, is due to CDW.

In a tunneling conductance (dI/dV) spectrum, known to represent the electronic density of states (DOS) of the sample surface, a gap sandwiched by two peaks, which is characteristic for quasiparticle DOS of superconductor, is observed (Fig. 2). The shape of the spectrum can be fitted well with the superconducting DOS formulated by BCS theory.

This apparatus enables us to study local electronic structure of various materials at < 100mK in nanoscale spatial resolution.

Reference
[1] E. Ishikawa, R. Shoda, N. Matsuura, M. Ono, T. Eguchi, A. Sakai, M. Kubota and Y. Hasegawa, e-Journal of Surf. Sci. and Nanotech., 2, 151 (2004) .

Authors
Y. Hasegawa, T. Eguchi, M. Kubota, and A. Sakai[a]
[a] International Innovation Center, Kyoto University

Thermal Stability of SrTiO$_3$ Surfaces

T. Ohnishi, M. Lippmaa, and Y. Matsumoto

Strontium titanate, SrTiO$_3$, is a perovskite-type oxide that is widely used as a substrate material for growing oxide thin films. In the field of oxide electronics, this material is also attracting attention due to its potential use as a semiconductor. Stoichiometric non-doped SrTiO$_3$ is an insulator with a band gap of 3.2 eV. The Fermi level, however, is close to the bottom of the conduction band and even slight doping will induce metallic conductivity and even low-temperature superconductivity.

Our main interest is in studying the properties of nanostructures or thin layers deposited on SrTiO$_3$ surfaces. In order to understand the transport and magnetic properties of such structures we need to know the atomic arrangement and the chemical composition of the interface layers. This task is greatly simplified if we can use an atomically well-ordered starting surface for our experiments.

Commercially available single-crystal SrTiO$_3$ substrates are typically polished and possibly wetetched to obtain a step-and-terrace surface morphology. Although the selectivity of the etching process ensures that the surface is perfectly terminated by the TiO$_2$ atomic layer, it does not produce a thermally stable surface. A recrystallization process of the surface starts at temperatures as low as 250 ˚C. The usual approach is to anneal the surface at close to 1000 ˚C until
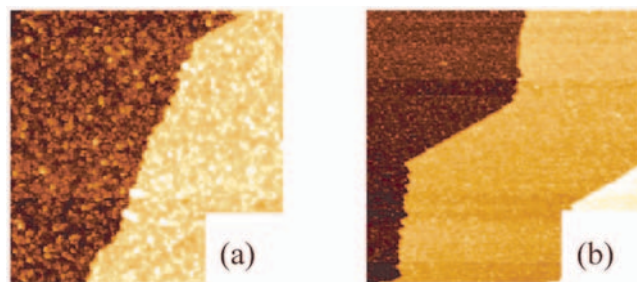

Fig. 1. Scanning tunneling microscope images of ex situ re-etched SrTiO$_3$ (001) surfaces after cleaning by heating at 300 ºC (a) and exposure to ultraviolet light (b). Image sizes are 250 nm x 250 nm. All step edges in the images have a height of a single unit cell.
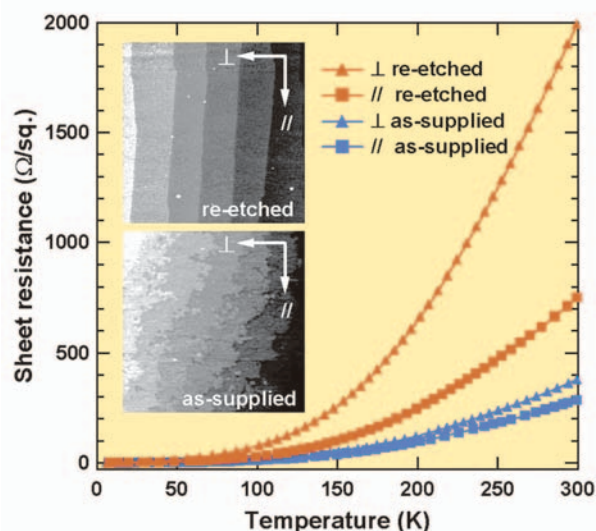

Fig. 2. Sheet resistance of 2 unit cell-thick LaTiO$_3$ films grown on a thermally stable Sr-free SrTiO$_3$ (001) surface (red) and on a commercial SrTiO$_3$ substrate (blue). The sheet resistance of the film grown on a Sr-free surface shows a large directional anisotropy. Resistance measured along surface step edges is lower than the value measured perpendicular to the step edges.

surface migration restores a regular step-and-terrace morphology. The drawback of this technique is that the annealed surface contains a small amount of segregated strontium, the precise amount of which is difficult to control. The segregated Sr at the interface works as an unintentional dopant in the interface layer.

We have developed a secondary etching procedure that can be performed after original high-temperature annealing. The etching time is very short and is intended only to remove selectively Sr from the SrTiO$_3$ surface. Suitable etchants are buffered HF acid or even warm water. We have shown that such surfaces are stable at up to 700 ˚C, which means that many heterointerface studies can now be performed on nearly ideal Ti-terminated surfaces. Heating a substrate above 300 ˚C after etching (Fig. 1a) is an effective way of removing contaminants from the crystal surface. Scanning tunneling microscope images show a nearly perfect surface structure after additional exposure to UV light (Fig. 1b). The terraces are atomically flat, all step edges have a height of one unit cell, and both the surface structure and the terminating layer remain stable up to 700 ˚C.

The importance of controlling the chemical composition of the substrate surface was studied by measuring the transport properties of 2 unit cell thick LaTiO$_{3+\delta}$ layers grown on SrTiO$_3$ surfaces. The films were grown at 700 ˚C. A non-annealed substrate would typically have a significant amount of segregated Sr present on the surface at this temperature. As expected, the transport behavior (Fig. 2, blue line) of the samples grown on non-annealed as-supplied substrates is similar to La$_{1-x}$Sr$_x$TiO$_{3+\delta}$. The films grown on an annealed and re-etched surface show a large drop in sheet resistance as a function of temperature and also a large directional anisotropy (Fig. 2, red line). This behavior is consistent with the presence of doped SrTiO$_3$ at the interface, either due to charge transfer from LaTiO$_3$ or due to the presence of oxygen vacancies. The directional anisotropy of resistance also shows that there is a large difference in conductivity along and across the surface steps.This work has clearly shown that careful control of the surface structure and composition of oxide single-crystal is extremely important for the design and characterization of heteroepitaxial

interfaces and nanostructures.

Authors
M. Lippmaa, T. Ohnishi, Y. Matsumoto[a], T. Ohsawa[a]
[a] Frontier Collaborative Research Center, Tokyo Institute of Technology

Itinerant Electron Metamagnetism and Magnetocaloric Effect

H. Yamada and T. Goto

Large magnetocaloric effects have recently been observed in 3d transition metal compounds MnFe(P,As) and La(Fe,Si)$_{13}$. These compounds exhibit a first-order transition of magnetization at the Curie temperature T_C. Above T_C, a metamagnetic transition (MT) takes place from the paramagnetic state to the ferromagnetic one under magnetic fields. Such a MT has been observed in many Co-based compounds [1]. These peculiar magnetic properties are well explained by the theory of itinerant-electron metamagnetism (IEM), where the effect of spin fluctuations is taken into account on the phenomenological Ginzburg-Landau theory [1]. In this report, magnetocaloric effects are discussed, based on the theory of IEM.

The equation of state for the magnetization M and magnetic field B is written by

$$B = a(T)M + b(T)M^3 + c(T)M^5$$

where $a(T)$, $b(T)$, and $c(T)$ are Landau coefficients renormalized by spin fluctuations as

$$a(T) = a(0) + (5/3)b(0)\xi(T)^2 + (35/9)c(0)\xi(T)^4$$
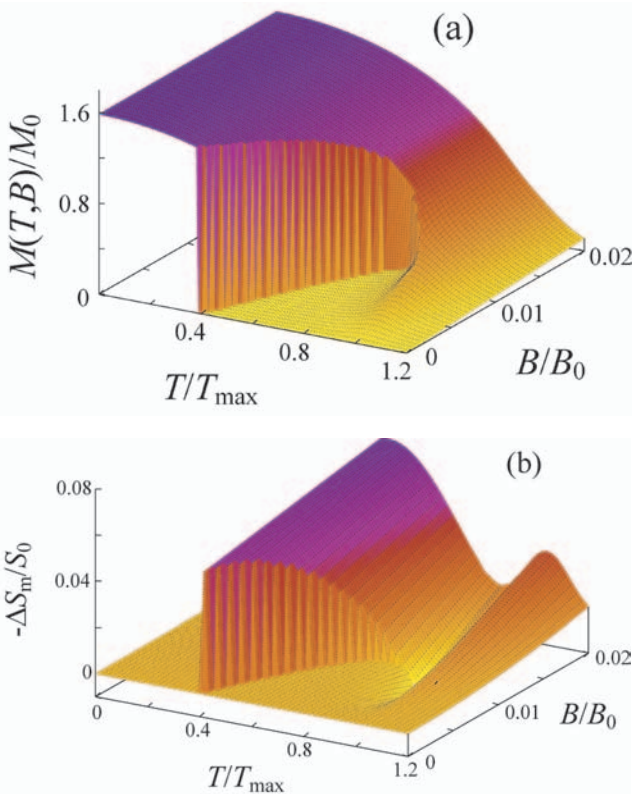$$b(T) = b(0) + (14/3)c(0)\xi(T)^2$$
$$c(T) = c(0)$$

Fig. 1. Calculated magnetization curve (a) and isothermal magnetic entropy change (b). M_0 and B_0 are those at the critical end point of MT ($a(0)c(0)/b(0)2=9/20$). $T/T_{max}=\xi(T)/\xi(T_{max})$. $S_0=B_0M_0/T_{max}$.
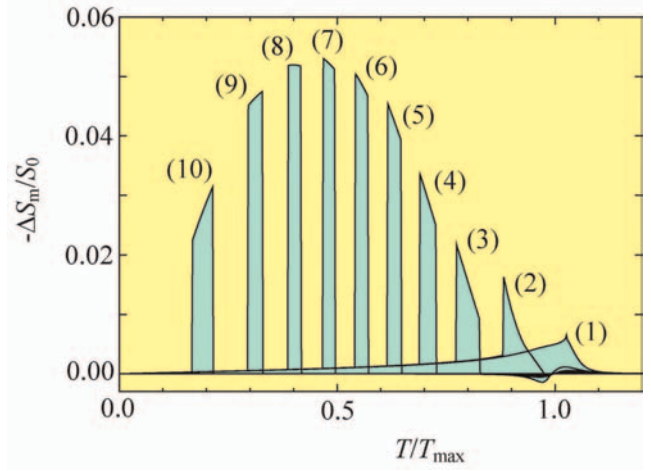

Fig. 2. Isothermal magnetic entropy changes $-\Delta S_m/S_0$ at $B/B_0 = 0.1 \times 10^{-2}$ Curves (1)-(10) are those for $a(0)c(0)/b(0)^2 = 0.178$-0.187 at an interval of 0.01.

where $\xi(T)^2$ is the mean square amplitude of spin fluctuations, which is well-known to increase as T^2 with increasing temperature T at low T. Then, the reduced temperature T/T_{max} is given by $\xi(T) / \xi(T_{max})$, where T_{max} is defined below.

The susceptibility $\chi(T)$ is given by $1/a(T)$. It is easily found when $a(0)>0$, $b(0)<0$, and $c(0)>0$ that $\chi(T)$ shows a maximum in its T-dependence at $\xi(T_{max})^2 = (3/14)|b(0)|/c(0)$. T_{max} is the susceptibility maximum temperature. It is also found that, when $a(0)>0$, $b(0)<0$, $c(0)>0$, and $3/16<a(0)c(0)/b(0)^2<9/20$, the ground state is paramagnetic and the MT takes place from $M=0$ to a finite M at a certain magnetic field. In this case, the critical field B_C is shown to increase as T^2 at low T, which is observed as a common property for itinerant electron metamagnets. When $5/28<a(0)c(0)/b(0)^2<3/16$, the ground state is ferromagnetic and $M(T)$ shows a first-order transition at T_C. The transition becomes second-order when $5/28>a(0)c(0)/b(0)^2$. The magnetic phase diagram is shown in [1].

The magnetization curves $M(T,B)$ can be calculated from the equation of state (1). Figure 1(a) shows the calculated $M(T,B)$ on the plane of T and B for $a(0)c(0)/b(0)^2=0.185$. At $B=0$, a clear first-order transition can be seen at $T/T_{max}=0.4$. Above T_C, the field-induced MT takes place at the critical field B_C. At the same time, the susceptibility maximum can be seen at high temperatures. This maximum grows up with increasing B, and connects smoothly with B_C of MT.

By the Maxwell relation the magnetic entropy change ΔS_m between $B=0$ and finite B is written by

$$\Delta S_m(T,B) = \int_0^B (\partial M(T,B')/\partial T)_{B'} dB'.$$

The calculated result of the isothermal magnetic entropy change is shown in Fig. 1(b). A large magnetic entropy change is seen at TC, associated with the first-order transition of the magnetization. More details about the magnetic entropy change based on the theory of IEM are given in [2].

In Fig. 2, the calculated results of the magnetic entropy changes $-\Delta S_m/S_0$ at $B/B_0 = 0.1 \times 10^{-2}$ for $a(0)c(0)/b(0)^2 = 0.178$-0.187 are shown . Negative and large entropy changes are obtained along the critical field B_C, while positive and small changes are obtained along B_{max} where $(\partial M(T,B)/\partial T)_B$ is positive. The trend of $-\Delta S_m/S_0$ as a function of T (Fig. 2) is a general one in itinerant electron metamagnets. More details of numerical calculations are given in [2].

References
[1] T. Goto, K. Fukamichi and H. Yamada, Physica B **300**, 167 (2001).
[2] H. Yamada and T. Goto, Phys. Rev. B **68**, 184417 (2003).

Authors
H. Yamada[a] and T. Goto
[a]Shinshu University

Possible One-dimensional ^{3}He Fermi Fluid Formed in Nanometer Pores of FSM-16

N.Wada and H.Ishimoto

Bulk ^{3}He liquid is known as a typical three-dimensional, 3D, Fermi fluid. Two-dimensional ^{3}He Fermi fluids have been produced on flat solid surfaces. Our purpose is to realize a new 1D ^{3}He Fermi fluid using a substrate with 1D nanometer pores. In the 1D pores of FSM-16 with diameter 2.8 nm, ^{4}He atoms form homogeneous layers on the pore walls up to the coverage of two atomic layers. Pre-plating with ^{4}He at the coverage of 1.47 layers, ^{3}He atoms are adsorbed on the 1D pore walls whose diameter ($2b$) is estimated to be about 1.8 nm. In this ^{4}He pre-plated nanopore, the ^{3}He atom adsorbed on the wall by a van der Waals potential has discrete energy levels in the cross section. The

energy gap Δ / k_B between the ground state and the first excited state is estimated to be about 0.34 K. Therefore if the Fermi energy $k_B T_F$ is sufficiently smaller than the gap energy Δ and $k_B T << (\Delta - k_B T_F)$, one can realize 1D ^{3}He Fermi degeneracy.

The heat capacity of the adsorbed ^{3}He was measured down to 5mK for small ^{3}He coverages n_3 that satisfy the 1D condition. The results are shown in the upper part of Fig.1, where the two lowest coverages (marked with solid and open circles) satisfy the 1D condition around the lowest temperature. Below about 50mK, all of the data approach to the T - linear dependence, which clearly indicates the Fermi degeneracy of the ^{3}He adatoms. The molar heat capacity C at the low coverage shows a maximum of about 1.5R (R : gas constant) around 0.1-0.15 K, and approaches to R corresponding to the 2D classical gas above about 0.4K. The heat capacity calculated for 1 D non-interacting gas is shown in the bottom of Fig.1 as a function of n_3 where T_F is marked with an arrow. The calculation at the low coverages reproduces the maximum around 0.1K as an essential character of the crossover from the low temperature 1D state to the high temperature 2D state. The maximum disappears when $k_B T_F$ approaches to the gap energy Δ at the higher coverages.

In conclusion, we have succeeded in realizing a 1D Fermi fluid in ^{3}He nanotube adsorbed on the ^{4}He pre-plated pores about 1.8 nm in diameter. At the lowest coverage it is a truely Fermi degenerated 1D system, because the motion in the cross section is in the ground state and there remains only one motional degree of freedom along the 1D pore.
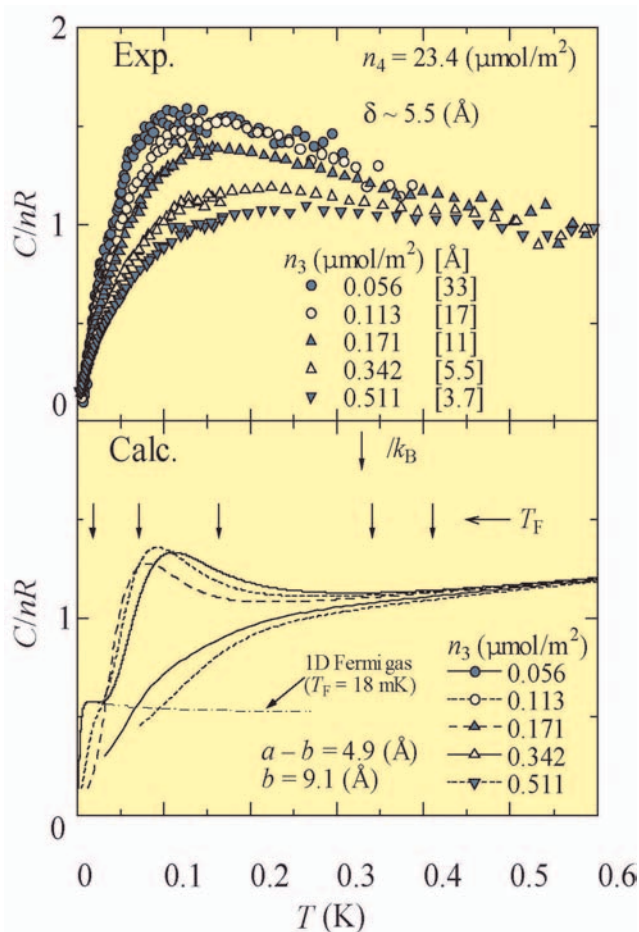

Fig. 1. (Upper): Molar heat capacities of ^{3}He adsorbed on the ^{4}He pre-plated 1D pores as a function of the ^{3}He coverage together with the mean inter-particle distance along the 1D pore. (Bottom): Calculated heat capacities of non-interacting gas in the 1D pore $2b$ =1.82nm in diameter.

The Low Temperature Phase Boundary of Pd-H$_x$ System

H. Araki, S. Harada, and M. Kubota

Particular interest has been focused on the peculiar physical properties of Pd-H(D)$_x$ systems at low temperature: the superconducting properties discovered in 1972 by Skoskiewicz[1] and the anomalous behavior of several physical properties of the hydride phase PdH$_x$ near 55 K. The latter is called the 55 K anomaly and was originally pointed out by Aston in 1957[2]. As to the specific heat measurements of Pd-H(D)$_x$ systems, there have been many reports. A lot of them, however, have been carried out with regard to the superconductivity of high hydrogen concentration regions at low temperature T < 10 K[3]. Other research interest was concentrated in the phenomena of the 55 K anomaly for x < 0.75[2]. The 55 K anomaly has been interpreted in terms of an order-disorder transition of the hydrogen sublattice. In the Pd-H$_x$ systems, two ordered structures have been shown as I4$_1$/amd and I4/m on the basis of neutron experiments for Pd-D systems[4]. The phase diagram of the Pd-H$_x$ system around 55K is expected to be rather complicated because of the long-range-ordering of hydrogen in Pd with a long relaxation time. Our present specific heat results, however, suggest a different phase diagram of hydrogen in palladium around this temperature.

We report systematic measurements of the specific heat of PdH$_x$ over a wide temperature range using a Pd specimen with higher purity than was used in our previous work[5].
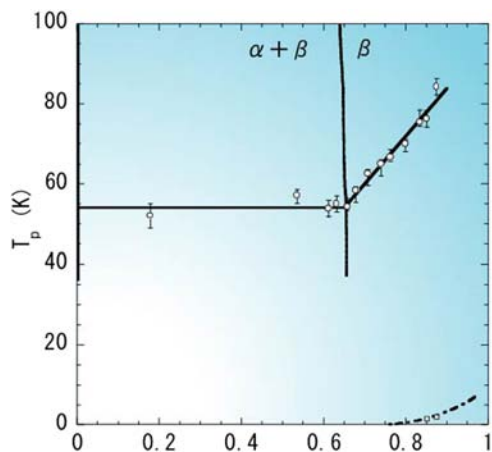
Fig. 1. Phase diagram for PdH$_x$. Open circles mean the T_p in this work, the solid lines are the new phase boundary: open squares and broken curve are the transition temperature of superconductivity.

With this specimen we could reproduce the concentration dependent superconducting transition for PdH$_x$ with $x > 0.8$. This is an important point because it can be difficult to determine the hydrogen concentration *in situ*, especially for higher concentration specimens. We describe a new phase diagram of hydrogen in palladium obtained using these careful procedures[6].

The specific heat for PdH$_x$ ($x = 0$ and 0.1777 to 0.8753) was measured between 0.5 K and 150 K by the quasi-adiabatic heat pulse method. The PdH$_{0.8753}$ and PdH$_{0.8514}$ specimens exhibited superconducting transitions at 2.0 K and 1.5 K, respectively. From these transition temperatures, we can confirm that the hydrogen concentration remained constant during measurements. The electronic specific heat coefficient and the Debye temperature for pure Pd and PdHx were evaluated by measured data from 3 K to 7 K. These values are in good agreement with the literature. Although the electronic state of PdH$_x$ changes with x, the Debye temperature of PdH$_x$ is hardly different from that of pure Pd. Because of the large mass difference of palladium and hydrogen, it is supposed that the hydrogen in the Pd lattice is vibrating independently. Therefore, it is assumed that the specific heat of PdH$_x$ can be expressed as the sum of contributions due to the lattice specific heat of Pd, the electronic specific heat of PdH$_x$, and the excess contribution caused by hydrogenation of the specimen. Two characteristic features are recognized in the excess specific heat converted into C$_{excess}$ per mole of hydrogen. One of them is the existence of a broad hump of specific heat which starts to appear from 10 K upwards independent of x. This hump can be interpreted as the change of the elastic properties of the matrix lattice caused by hydrogenation of Pd.

The other is the existence of mirror-λ shape's specific heat. The sharp peak which indicates a phase boundary with transition temperature $T_p = 55$ K to 85 K depending linearly on the hydrogen concentration from $x = 0.6572$ to 0.8753. We do not observe anomalies at specific x values as would be expected for the specific ordered structures.

In this study, we have reported here the specific heat measurements of PdH$_x$ over the wide temperature range 0.5 K < T < 100 K in the high hydrogen concentration region where the superconductivity transition was observed. The obtained phase diagram of hydrogen in Pd shown in the figure indicates new features which are not consistent with an order-disorder phase transition between two ordered structures, but are consistent with other measurements.

Because of the large diffusion coefficient, when the density of the H/D is increased in Pd, we may expect some macroscopic quantum phenomena because of overlapping of the wave function below some temperature. It should differ depending on the Fermi and/or Bose statistics of the hydrogen atoms. And the phase diagram may be modified when the quantum nature becomes stronger as is seen in Helium isotopes phase diagrams. In order to further clarify this phase boundary, specific heat measurements are being prepared for the PdD$_x$ system in order to check if the phase boundary has to do with quantum statistics, and further investigation will be required.

References
[1] T. Skoskiewicz, Phys. Status Solidi **a11**, K123 (1972).
[2] D. M. Nace and G. J. Aston, J. Am. Chem. Soc. **79**, 3627 (1957).
[3] C. A. Mackliet *et al.*, J. Phys. Chem. Solid **37**, 379 (1976).
[4] O. Blaschko, J. Less-Common Met. **100**, 307 (1984).
[5] H. Araki *et al.*, Physica B **284-8**, 1255 (2000).
[6] H. Araki *et al.*, J. Low Temp. Phys. **134**, 1145 (2004).

Authors
H. Araki[a], M. Nakamura[b], S. Harada[b], and M. Kubota
[a]Nagaoka National College of Technology.
[b]Fac. Eng. Niigata Univ.

Pinning of Vortices of Rotating B-like Phase in Superfluid ^{3}He Confined in 98 % Aerogel

O. Ishikawa and M. Kubota

The vortex in fluids is an interesting phenomenon, such as in turbulence in many fluids. Especially, when the fluid is quantum liquid, the vortex has a circulation quantum and is often called a vortex line. When you rotate a sample cell, a vortex cluster composed of many straight vortices is formed in the middle part of the cell and creates the superfluid velocity field of rigid body rotation in the cluster region. The cluster of vortices itself rotates with the sample cell. Stopping rotation makes a vortex cluster unstable and no vortex remains.

Such a vortex motion in bulk liquid is drastically changed by existing Aerogel, which is made of tangling silica strands of a few nm in diameter with a large porosity more than 90%. The diameter of strand is much shorter than the coherence length of superfluid ^{3}He, a few tens of nm, but the average distance between strands is comparable with the coherence length. So the coherence of superfluidity is not completely destroyed and Aerogel plays as impurity. Recently the first rotating experiment on superfluid ^{3}He in Aerogel was performed in the ultra low temperature group at ISSP [1].

In Fig. 1, NMR absorption curves are shown at several rotating speeds. The reason why the NMR signal changed by rotation was that the large counter-flow between v$_n$ and v$_s$ changed the relative orientation of order parameter vector to the magnetic field. The large rotating speed made the increase of absorption in higher frequency region and the decrease in lower frequency region simultaneously in Fig. 1(a). But at a speed in deceleration from the maximum angular velocity, NMR spectra was almost the same as that before rotation and in further deceleration the same change for the large rotating speed appeared even at rest in Fig.
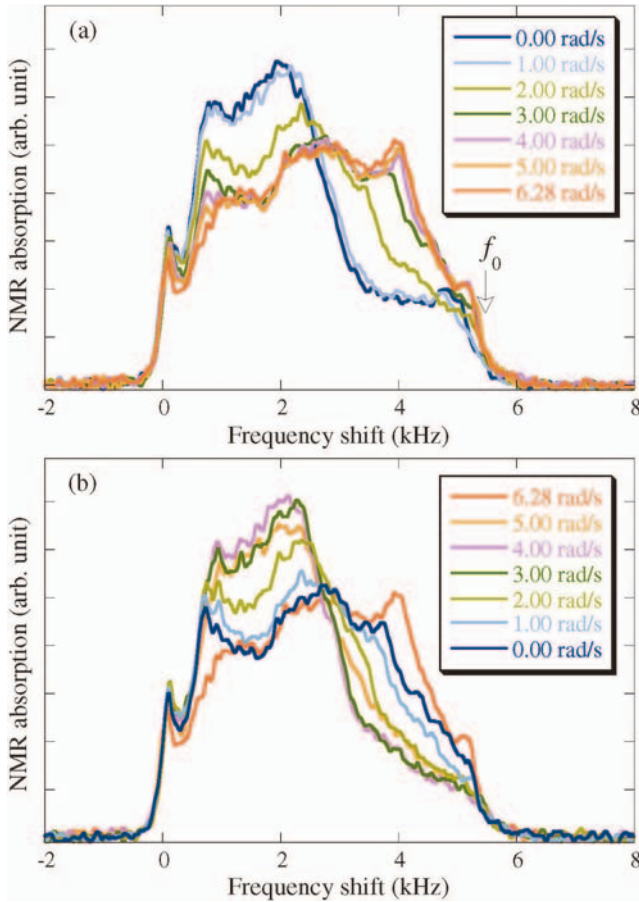
Fig. 1. Rotation dependence of NMR spectra at T = 0:67 T$_c$ in acceleration (a) and in deceleration (b).

1(b). This means existing of a large counter-flow at rest. Only the superfluid velocity should remain in aerogel because the normal fluid velocity at rest should be zero in the whole cell.

From the NMR spectrum we can obtain the intensity of counter-flow. which is shown as a function of Ω in Fig. 2. When the angular velocity once exceeded Ω_c, the hysteresis was observed. Such a hysteresis curve is observed in the hard type II superconductor as a result of vortex pinning [2]. Keeping the superfluid velocity finite while cryostat stays at rest is due to the pinning of vortices in Aerogel. The mechanism of pinning of vortex in superfluid ^{3}He by Aerogel is not so clear that we can only mention the inhomogeneity of Aerogel density may be responsible for the pinning center. We think that the instability mechanism for vortex motion
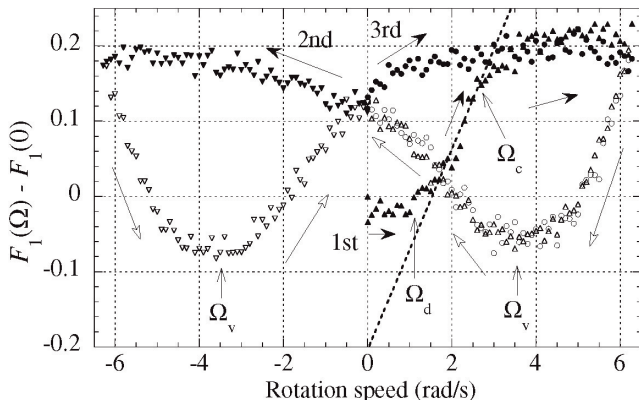

Fig. 2. Rotation dependence of the counterflow intensity at T = 0:67 T$_c$. Ω_c = 2:6 rad/s is the critical velocity of the vortex penetration into the aerogel.

introduced by Glaberson and Donnely [3] is applicable to explain how the vortex density redistributes.

References

[1] M. Ymashita, J. Low Temp. Phys. 134, 749 (200).
[2] C. P. Bean, Rev. Mod. Phys. 36, 31 (1964).
[3] W.I.Glaberson and R.J.Donnely, Phys.Rev. 141, 208 (1960).

Authors
M. Yamashita, A. Matsubara, R. Ishiguro, Y. Sasaki, Y. Kataoka, M. Kubota, O. Ishikawa, Y. M.Bunkov, T. Ohmi, T. Takagi, and T. Mizusaki

Tunnel Magnetoresistance of Co-Al-O Granular Films under High Pressure

S. Kaji, G. Oomi, and Y. Uwatoko

In granular films consisting of ferromagnetic metal Co granules of nanometer size (2-3 nm) in an insulating matrix, which includes the randomly oriented magnetic moments, the conduction of electrons is well known to be dominated by the tunneling between the granules. Since the electron tunneling in these materials depends on the relative orientation of magnetic moments between ferromagnetic granules (spin-dependent tunneling), it gives rise to the large tunnel magnetoresistance(TMR) of the order of 10 %. Such films have a large number of granules with a broad distribution of size. The distribution and the Coulomb blockade have been shown to play an important role in TMR. Furthermore, higher-order tunnel conduction has been pointed out to show a significant effect on the magnitude of TMR in the low temperature[1,2].

The TMR in insulating Co-Al-O granular films has been studied under high pressure up to 3 GPa[3]. It is found that the pressure enhances the TMR at 4.2 K and its effect depends on temperature. The results provide clear evidence that the successive onset of higher-order processes in tunneling conduction at low temperature below ca. 50 K, which is affected by strong Coulomb blockade, is enhanced at high pressure. In order to clarify the effect of pressure on the TMR above 3 GPa more precisely, we made an attempt to measure the magnetoresistance(MR) of Co-Al-O fims up to 8 GPa in the wide range of temperature.

Figure 1 shows the MR ratio at 4.2 K defined as MR = $(\rho(H) - \rho_{max})/ \rho_{max}$, where ρ_{max} is the maximum resistivity around zero field. The maximum in $\rho(H)$ curve at 4.2 K is observed around the coercive force H_c. The MR ratio increases from 13.8 % to 14.5 % as pressure increases
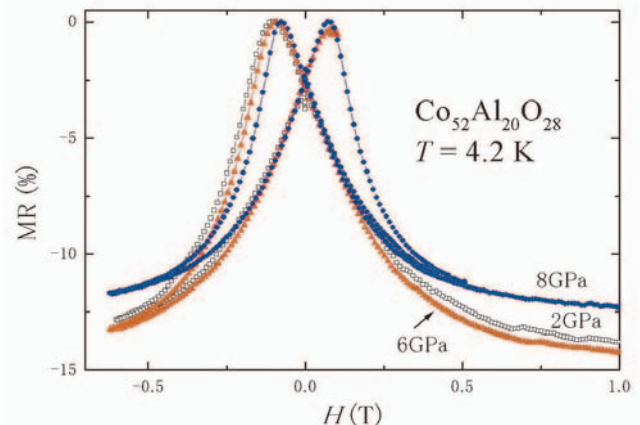

Fig. 1. MR curves measured at 4.2 K under high pressure. The vertical axis indicates the values of $\Delta\rho / \rho_{rmax}$, $\Delta\rho = \rho(H) - \rho_{max}$.
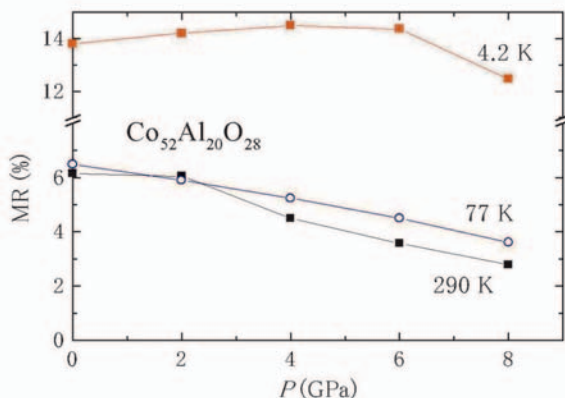
Fig. 2. Pressure dependence of the MR ratio at 4.2 K, 77 K and R.T..

below 6 GPa, but the MR ratio decreases above 6 GPa. The H_c decreases at the rate, $dHc / dP = - 4.3 \times 10^{-3}$ T / GPa.

Pressure dependence of MR at R.T., 77 K and 4.2 K is shown in Fig. 2. It is found that the behavior of MR against pressure is different depending on the temperature. The MR in high temperature range, R.T. and 77 K, decreases monotonously with pressure approximately in the linear fashion and the behaviors are nearly the same. The decreasing rate $1/MR_T$ ($\partial(MR_T) / \partial P$) at $T = 77$ K and R.T. are $- 7.1 \times 10^{-2}$ GPa^{-1} and $- 5.4 \times 10^{-2}$ GPa^{-1}, respectively. On the other hand, the pressure coefficient of MR at 4.2 K changes its sign from positive to negative with increasing pressure, *i.e.*, it shows a broad peak centered around 5 GPa. This result indicates that the higher order tunneling effect is suppressed above 5 GPa because it becomes significant at low temperatures below 50 K. The magnitude of MR is approximated by the following equation, MR $\approx$ (n* + 1)σ^2, where n* is related to a number of Co granules on a conduction path and σ is the spin polarization. In the previous study[3], it has been revealed that n* increases with pressure by the enhancement of higher order tunneling at high pressure. But above 3 GPa the effect of pressure dependence of σ, which decreases with pressure, may not be neglected anymore. This is the origin of the broad peak in the pressure dependence of MR at 4.2 K. On the other hand, the TMR at 77 K and room temperature decreased as pressure increased. This result is well explained by considering that the pressure change in σ becomes predominant at *r.t.* or 77 K since the higher order effect is suppressed or the contribution from n* is relatively small.

Thus the large difference in the pressure dependence of TMR between at 4.2 K and at R.T. or 77 K is consistently explained by using the pressure dependence of n* and σ.

Reference
[1] S. Takahashi and S. Maekawa, Phys. Rev. Lett., **80**, (1998) 1758.
[2] S. Mitani, S. Takahashi, K. Takanashi, K. Yakushiji, S. Maekawa and H. Fujimori: Phys. Rev. Lett. , **81**, (1998) 2799.
[3] S. Kaji, G. Oomi, S. Mitani, S. Takahashi, K. Takanashi, S. Maekawa, Phys. Rev. B, **68**, (2003), 054429.

Authors
S. Kaji[a], G. Oomi[a], S. Mitani[b], S. Takahashi[b], K. Takanashi[b], S. Maekawa[b], M. Hedo, and Y. Uwatoko
[a]Dept. of Phys., Kyushu University
[b]Institute for Material Research, Tohoku University

Development of the High Field ESR System under Pressure

T. Sakurai and Y. Uwatoko

We have developed a new system which enables ESR measurements under pressure [1, 2]. Although there are some types of X-band ESR system under pressure, our system has advantages that the high magnetic field up to 16 T obtained by the pulse technique and wide frequency range from 70 GHz to at least 460 GHz are available. In addition to these advantages, a characteristic pressure cell for our ESR system is used and a unique pressure-calibration method has been established as described below.

A clamped-type pressure cell is used for the high field ESR system. The inner parts such as pistons are made from sapphire because millimeter and submillimeter electromagnetic wave must be transmitted. The cylinder is made from CuBe alloy with the inner and outer diameter of 3 mm and 6 mm, respectively. The pressure can reach 3.5 kbar and it is limited by the ratio of the inner and the outer diameters. The outer diameter is determined by the bore of the solenoid magnet. On the other hand, the inner diameter favors above 3 mm because the signal intensity directly depends on the amount of the sample. We are now examining a new cylinder made from NiCrAl alloy with almost the same design and try to achieve the higher pressure.

Next, the pressure-calibration method for ESR measurements will be described. Figure 2 shows typical ESR spectra of ruby under ambient pressure and under pressure. Ruby includes a small amount of Cr^{3+} ion. Cr^{3+} ion has the trigonal symmetry and the spin is $S = 3/2$. The spin-Hamiltonian of ruby is described as g$\mu_B SH + DS_z^2$, where g is the g-factor, H is the magnetic field and D is the single ion anisotropy. When the magnetic field is applied parallel to the *c*-axis, which corresponds to the z-axis in the spin-Hamiltonian, the resonance fields are obtained to be $H_a = (h\nu + 2D)/g\mu_B$, $H_b = h\nu/g\mu_B$ and $H_c = (h\nu - 2D)/g\mu_B$. As shown in Fig. 1, three absorption lines with almost the same intervals are observed. The resonance field H_a shifts to the lower field side and the resonance field H_c shifts to the higher field side by applying the pressure, while the resonance field H_b does not shift. These results show that the absolute value of D increases under pressure. We obtain the
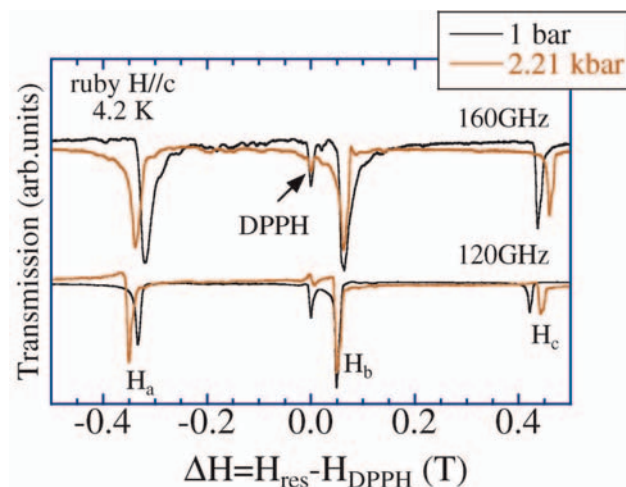

Fig. 1. Typical ESR spectra of ruby at 1 bar (black) and at 2.21 kbar (red). The horizontal axis is normalized by the resonance position of the DPPH, where DPPH is the magnetic field marker. Three signals H_a, H_b and H_c due to ruby are observed and H_a and H_c shifts under pressure while H_b does not change.
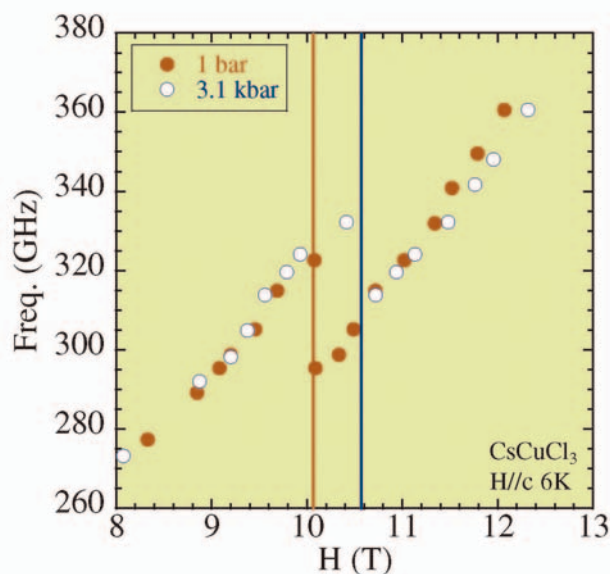
Fig. 2. Frequency-field diagram of CsCuCl₃ at 6 K for H//c. The discontinuous change of ESR mode indicates the magnetic phase transition. The transition field shifts to the higher field side under pressure.

first differential coefficient as -4.3×10^{-2} GHz/kbar at 4.2 K below 3 kbar and this value can be used to calibrate the pressure by setting ruby with a sample at the same time.

Finally, we demonstrate an example of high field ESR measurement under pressure. Figure 2 shows the frequency-field diagram of $S = 1/2$ quantum spin system CsCuCl₃ which is a well-known triangular antiferromagnet [2, 3]. Below the antiferromagnetic transition temperature T_N = 10.5 K, the spins form 120° structure in the c-plane [4]. This compound shows a small jump in the magnetization process when the magnetic field is applied parallel to the c-axis. It is shown by the theoretical studies that this jump in the magnetization process corresponds to the magnetic phase transition from the "umbrella-type" spin configuration to the "collinear-type" spin configuration induced by the quantum fluctuation [5]. The discontinuous change of ESR mode in Fig. 2 reflects the magnetic phase transition and the transition field H_c is found to shift to the higher field side by applying the pressure. We analyzed this change of ESR mode within the mean field approximation. As a result it is concluded that one of the key parameters is the easy-plane type anisotropy of this system and we found this anisotropy energy increases under pressure. Theoretically, the anisotropy is considered to compete with the quantum fluctuation and to stabilize the "umbrella-type" spin configuration [5]. These facts support the experimental results that the increase of the transition field H_c under pressure is related to the increase of the easy-plane type anisotropy.

References
[1] H. Ohta, *et al.*, J. Phys.: Condens. Matter **14** (2002) 10637.
[2] T. Sakruai, *et al.*, J. Phys. Soc. Jpn. **72** (2003) Suppl. B 156.
[3] T. Sakruai, *et al.*, Physica B **346-347** (2004) 221.
[4] K. Adachi, *et al.*, J. Phys. Soc. Jpn. **49** (1980) 545.
[5] T. Nikuni and H. Shiba, J. Phys. Soc. Jpn. **62** (1993) 3268.

Authors
T. Sakurai[a], H. Ohta[b], and Y. Uwatoko
[a]Center for Supports to Research and Education Activities, Kobe University.
[b]Molecular Photosience Research Center, Kobe University.

Time-Resolved Auger Decay in CsBr by Using High Harmonics

T. Shimizu, M. Itoh, and S. Watanabe

A vacant state in an inner-shell relaxes with time constants ranging from a few attoseconds to a few femtoseconds, depending on the binding energy. The inner-shell holes created vanish through an ultrafast rearrangement of the electronic system, leaving two holes in the outer levels. This process, known as an Auger process, is a universal phenomenon in atoms, molecules, and condensed matter. The lifetime of core holes has been estimated from the full width at half maximum of the photoelectron spectra. However, spectral measurements can provide only indirect information on the Auger decay process. Real time measurements are greatly needed to study Auger dynamics. The time-resolved spectroscopy of core holes needs high temporal resolution along with high photon energy to excite the inner shell. High harmonics (HH) of a femtosecond laser have a pulse width down to sub-fs in the extreme-ultraviolet and soft x-ray regions. Therefore, HH are eminently suitable for time-resolved spectroscopy following core hole creation.

In condensed matter, interatomic Auger transitions are possible among neighboring atoms. Such interatomic Auger processes could be largely affected by the environment of created holes, such as lattice deformation or vibration (i.e., temperature or injected carrier density), and are a challenging subject in solid-state physics. CsBr is of special interest for the study of the Auger process, because it has two competing relaxation channels of holes created in the Cs⁺ $5p$ outermost-core band, radiative decay and nonradiative Auger decay. At low temperatures, Auger decay is energetically forbidden because the energy difference E_{VC} between the top of the outermost core band and the top of the valence band is smaller than the band gap energy E_g. However, the Urbach exciton tail states can provide suitable final states for Auger decay products, causing the rate to increase with temperature. In the present experiment, we measured the temperature-dependent decay time of the luminescence arising from the radiative decay of Cs⁺ $5p$ core holes, and determined the Auger decay probability at the high-temperature limit. Figure 1 shows the temperature dependence of the decay time of the luminescence. The interatomic Auger decay time was, for the first time, estimated to be 2.4+3.8/-1.5 fs in condensed matter, in good agreement with a theoretical calculation of alkali halides. The present work veri-
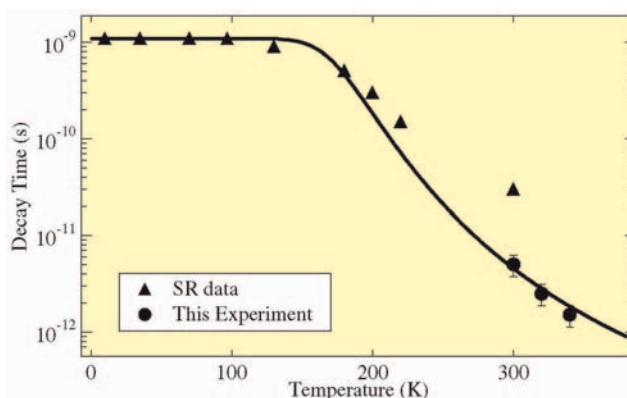

Fig. 1: Temperature dependence of the decay time of the luminescence in CsBr. Closed triangles correspond to the data obtained by SR and closed circles to the present data. Solid line is the best fit of a theoretical model to the experimental result.

fied that HH enable time-resolved spectroscopy with high temporal resolution that was not accessible before by synchrotron radiation (SR).

Reference
[1] T. Shimizu, T. Sekikawa, T. Kanai, S. Watanabe, and M. Itoh, Phys. Rev. Lett. **91**, 017401 (2003).

Authors
T. Shimizu, T. Sekikawa, T. Kanai, S. Watanabe, and M. Itoh[a]
[a] Department of Electrical and Electronic Engineering, Shinshu University

Unoccupied Electronic Structure of Lightly-Doped SrTiO₃ by Resonant-Inverse Photoemission Spectroscopy

T. Higuchi and S. Shin

Recently, there has been a renewed interest in the electronic structure of $SrTiO_3$ doped with charge carrier. When a small number of electrons chemically doped into $SrTiO_3$, e.g. by La^{3+} substitution for Sr^{2+} site or by Nb^{5+} substitution for Ti^{4+} site, the doped electrons enter the bottom of the empty Ti $3d$ band. In the limit of lightly doping concentration, there will be no electron correlation between the doped electrons since the probability of electron-electron scattering is vanishingly small. The photoemission spectra have two features in the band gap region, which are generally believed to be a coherent part at the Fermi level (E_F) and an incoherent part at ~1.5 eV that is attributed to a remnant of the lower Hubbard band. The band structure calculations that assume a rigid-band filling cannot reproduced the peak at ~1.5 eV, though the bandwidth of O $2p$ valence band shows a good agreement with the photoemission spectra. The origin of the ~1.5 eV peak has been studied by several theoretical calculations. It is proposed that the ~1.5 eV peak is contributed to be a polaronic feature or a surface structure that is created due to the degree of correlation and disorder in the surface. A similar feature is also expected in the conduction band side.

In this paper, we present resonant inverse-photoemission spectroscopy (RIPES) spectra of lightly Nb-doped $SrTiO_3$ ($SrTi_{0.98}Nb_{0.02}O_3$). The RIPES is a powerful technique to investigate the unoccupied electronic structure in the surface state. Although the technique and new physics obtained from RIPES spectra were investigated in rare-earth metal compounds by Kanai et al.[1], the RIPES spectra of lightly $3d$ transition metal compounds has not been reported thus far.

Figure 1 shows the excitation energy dependence of the RIPES spectra of $SrTi_{0.98}Nb_{0.02}O_3$ in the incident electron energy (E_K) region of Ti $3p$ core level. The abscissa represents the energy above the Fermi level (E_F) that was calibrated by the Fermi edge of Au. The intensity of the feature D at about ~7.3 eV becomes strong at lower E_K. This is considered to be due to the electron energy dependence of the ionization cross section, indicating the existence of the Sr $4d$ band. The broad bands indicated by arrow are the normal Ti $3p$ fluorescence that is caused by the Ti $3p$ core hole created by the electron excitation. In the energy region from 0 to 5 eV, two prominent features A and B are found at ~1.7
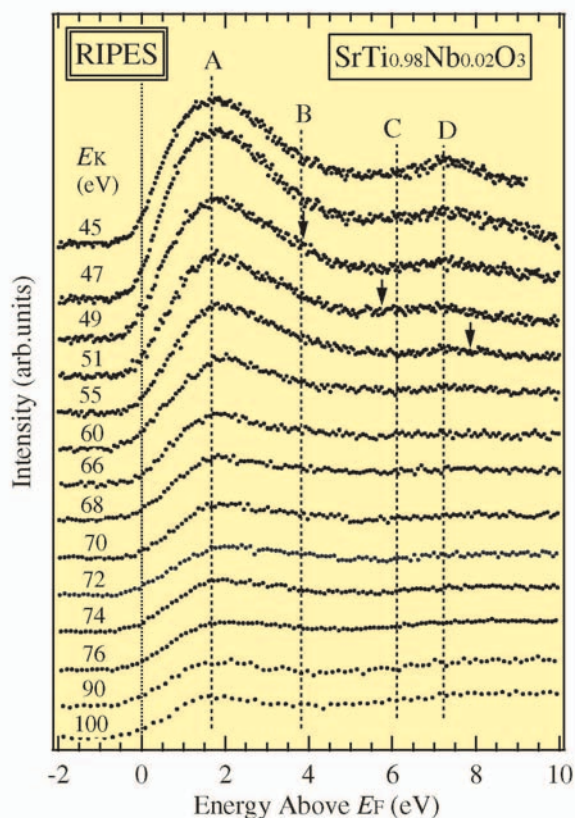

Fig. 1. IPES spectra of $SrTi_{0.98}Nb_{0.02}O_3$ near the Ti $3p \rightarrow 3d$ absorption edge measured by various kinetic energy of the incident electron (E_k). The abscissa is the energy above Fermi level (E_F=0 eV). Arrow shown in each spectrum indicates the normal fluorescence.
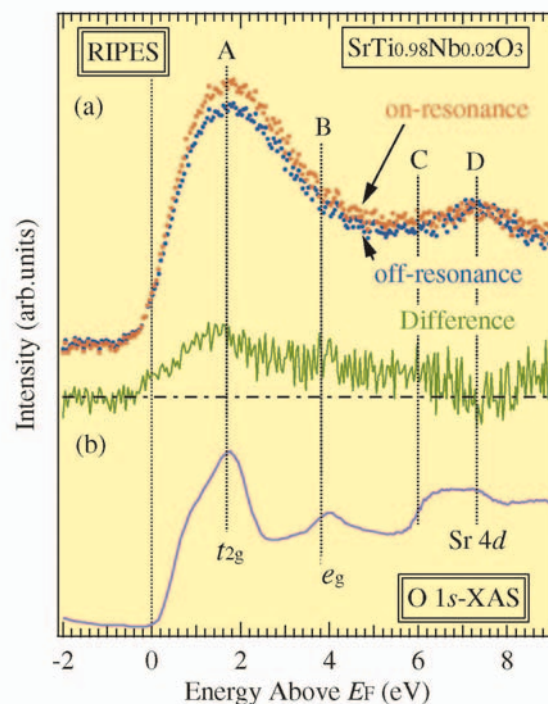

Fig. 2. (a) On-resonance (red circle) and off-resonance (blue circle) spectra measured at E_k= 47 eV and 45 eV, respectively. Difference spectrum (green line) subtracted from on- and off-resonance spectrum is also shown. (b) O $1s$ XAS spectrum.

and ~3.9 eV, respectively. The intensities of the features A and B increase with decreasing E_K and decrease at E_K=45 eV. This indicates the resonance effect of the RIPES spectra at E_K=47 eV.

Figure 2(a) shows the comparison of on- and off-resonance spectra of the conduction band measured at E_K= 47 and 45 eV. One can find that the Ti $3d$ components in both the features A and B are resonantly enhanced by the Ti $3p \rightarrow 3d$ excitation in the on-resonance spectrum, though the resonance effect of the feature B is very weak in comparison with that of the feature A. The difference spectrum from on-resonance to off-resonance spectra is also shown. The difference spectrum corresponds to the Ti $3d$ partial density-of-state (DOS) in the conduction band. The O $1s$ X-ray absorption spectrum of $SrTi_{0.98}Nb_{0.02}O_3$ is also shown in Fig.2 (b). The energy position of Sr $4d$ state of the O $1s$ X-ray absorption spectroscopy (XAS) spectrum matches with the broad band at ~7.3 eV (feature D) in the RIPES spectra. On the other hand, two features at ~1.7 eV and ~3.9 eV of O $1s$ XAS spectrum reflect the t_{2g}- and e_g-subbands of the Ti $3d$ states. It is striking that the energy positions of the t_{2g} and e_g subbands of O $1s$ XAS spectrum are good agreement with the features A and B of the RIPES spectra, as shown in two vertical dashed lines. These positions of the features A and B mismatch with those of the coherent and incoherent parts, which are expected from the disordered Hubbard model [2].

In the difference spectrum of Fig.2 (b), the feature C at ~6.1 eV, which show the Ti $3p \rightarrow 3d$ resonant effect in Fig.2, does not match with the O $1s$ XAS spectrum. The existence of the feature C might be attributed to the surface-induced structure, because the O $1s$ XAS spectrum is the bulk sensitive. In recent years, the band structure in the conduction band region of the lightly-doped $SrTiO_3$ has been calculated by Sarma *et al* [2]. They used the linearized muffin-tin orbital method within the atomic-sphere approximation. From the second order perturbation applied to the DOS obtained from LMTO supercell calculation, a correlation-induced satellite appears outside the one-electron bandwidth in the unoccupied states. The energy position of the correlation satellite structure matches with that of the feature C. This fact indicates that the correlation effect exists in the surface state of lighly-doped $SrTiO_3$ [3].

References
[1] K. Kanai and S. Shin, J. Electron Spectrosc. Relat. Phenomn. **117-118** (2001) 383.
[2] D. Sarma, S. R. Barman, H. Kajueter and G. Kotliar, Europhys. Lett. **36** (1996) 307.
[3] T. Higuchi, S. Nozawa, T. Tsukamoto, R. Eguchi, H. Ishii, Y. Tezuka, S. Yamguchi, K. Kanai, and S. Shin, Phys. Rev. B **66** (2002) 153105.

Authors
T. Higuchi,[a] T. Tsukamoto,[a] K. Kanai,[b] Y. Tezuka,[c] R. Eguchi, and S. Shin
[a] Department of Applied Physics, Tokyo University of Science
[b] Department of Chemistry, Nagoya University
[c] Department of Electronic and Information System Engineering, Hirosaki University

Electronic Structure and its Contribution to Large Thermoelectric Power in Layered Cobalt Oxides

T. Takeuchi and S. Shin

Layered cobalt oxides characterized by two-dimensionally spanned CoO_2 triangular-lattice consisting of edge-shared CoO_2 octahedrons have attracted a great deal of interests because of their possession of unusual electrical properties[1-3]. Large thermoelectric power simultaneously observed with metallic electrical conduction is especially important from the technological point of view because the large thermoelectric power (S) and the large electrical conductivity (σ) together with a low thermal conductivity (κ) are of necessities for the development of a practical thermoelectric material that has been regarded as one of the key technologies of energy-saving and environmental protection.

In the present study, electronic structure in the γ-phase $Na_{0.6}CoO_2$, $Bi_2Pb_2Co_2O_9$, and $Ca_3Co_4O_9$ is investigated in detail using high-resolution ultraviolet photoemission spectroscopy (UPS) and Co $2p$-$3d$ resonant photoemission spectroscopy (RPES). The electron transport properties of both electrical conductivity and thermoelectric power for these layered cobalt oxides and their sample dependence are discussed in terms of the measured electronic structure near the Fermi level E_F, and the specific electronic structure responsible for the metallic electrical conduction and the large thermoelectric power is experimentally investigated. The temperature dependence of the thermoelectric power $S(T)$ was calculated from the measured electronic structure within the context of the Boltzmann transport equation. We demonstrate that the large thermoelectric power in the layered cobalt oxides can be well accounted for in terms of the Boltzmann-type metallic conduction in a narrow band specific to the two-dimensional CoO_2 layers.

Figure 1 shows the Co $2p$-$3d$ on-resonant and off-resonant photoemission spectra accumulated at $hv =$ 778 eV and 771 eV, respectively. The off-resonant spectra of all these compounds exhibit an intense peak at ~1.0 eV below E_F. We consider that the electronic states causing this intense peak are closely related with their possession both of the
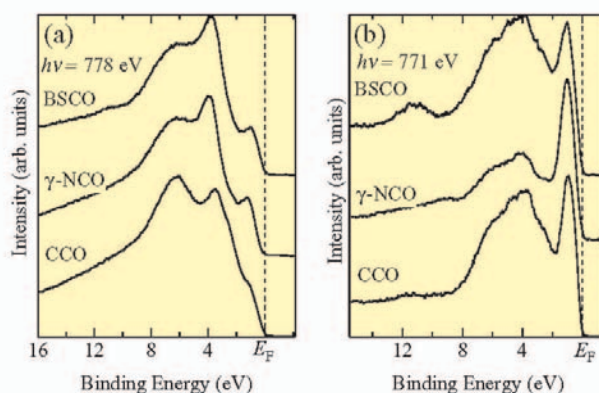

Fig. 1. (a) Co $2p$-$3d$ on-resonant spectra of $Ca_3Co_4O_9$ (CCO), $Bi_2Sr_2Co_2O_9$ (BSCO) and γ-$Na_{0.6}CoO_2$ (γ-NCO) measured with an incident energy of $hv =$ 778 eV at 20K. (b) Off-resonant XPS spectra of CCO, γ-NCO, and BSCO measured at 20K. All spectra are characterized by an intense peak centered at ~ 1 eV. The Fermi level is located near the high-energy edge of this peak.
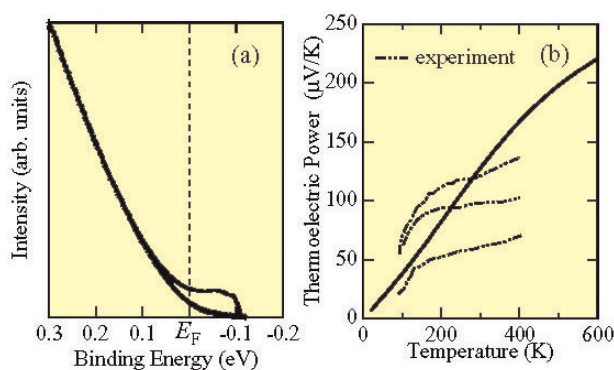
Fig. 2. (a) UPS spectra at 300K (+) and those divided by the Fermi-Dirac distribution function (UPS/FD spectra; with thin lines) are shown for $Bi_2Sr_2Co_2O_9$ (BSCO). The density of states above E_F is revealed in the UPS/FD spectra. The UPS/FD spectra were used as $N(E)$ for the evaluation of thermoelectric power. The deduced thermoelectric power are shown in (b) with the experimentally observed data. A positive temperature coefficient and large positive value of the thermoelectric power of the $Bi_2Sr_2Co_2O_9$ was reproduced.

large thermoelectric power and metallic conduction, because E_F is located near the high-energy end of this peak. However, this peak turned out to be less obvious in the on-resonant spectra, though the intensity itself was increased more than five times larger due to the Co $2p$-$3d$ resonance. This means, thereby, that the band(s) lying in the energy range from E_F to 2.0 eV below E_F consists both of the O $2p$ and Co $3d$ components, and is dominated more by O $2p$ component than by the Co $3d$ component.

The density of states at E_F is finite but negligibly small at room temperature because E_F is located near the high-energy edge of this narrow band. Since thermoelectric power is inversely proportional to the density of states at E_F, one may naturally expect that this characteristic electronic structure would be responsible for the large thermoelectric power of these layered cobalt oxides. We calculated thermoelectric power $S(T)$ using the Boltzmann transport equation with the electronic structure near E_F determined by the high resolution UPS measurement. The calculated $S(T)$ shows fairly good consistency with the measured value both in its magnitude and the temperature dependence. We conclude, therefore, that the large thermoelectric power observed in these layered cobalt oxides can be explained within the framework of the Boltzmann-type electrical conduction mechanism and the electrons in the narrow band with its band edge near E_F. Detailed results were reported elsewhere [4].

References
[1] K. Takeda et al., Nature **422**, 53 (2003).
[2] T. Valla *et al*., Nature **417**, 627 (2002).
[3] I. Terasaki *et al*., Phys. Rev. B **56**, R12685 (1997).
[4] T. Takeuchi *et al*., Phys. Rev. B **69**, 125410 (2004).

Authors
T. Takeuchi[a], T. Kondo[b], U. Mizutani[b], S. Tsuda, T. Kiss, T. Yokoya, and S. Shin
[a] Ecotopia Science Institute, Nagoya University.
[b] Department of Crystalline Materials Science, Nagoya University.

Strain Field under the SiO_2/Si(001) Interface Revealed by the Phase-sensitive X-ray Diffraction Technique

W. Yashiro, K. Miki, and T. Takahashi

Strain near an interface affects its electronic structure, but a full understanding of such strains is still lacking even in the case of SiO_2/Si, which has been applied to electronic devices since 1960s. We have developed a new technique, the phase-sensitive X-ray diffraction (PSXD) technique, which is a powerful way to characterize strain fields near crystal surfaces, and applied it to a Si(001) wafer whose surface is covered with a thermal oxide layer [1]. It was revealed that there is a small strain field distributing over mesoscopic-range depth (up to several hundred of nm) under the SiO_2/Si interface and having a static fluctuation in lateral direction.

The PSXD technique is an application of a phenomenon, modulation of the intensity of the crystal-truncation-rod (CTR) scattering under an excitation of a Bragg reflection [1,2], which is an interaction between a two-dimensionally diffracted wave (CTR scattering) and a three-dimensionally diffracted (Bragg reflection) wave. An example of the phenomenon in the case of the Si(001) wafer is shown in Fig. 1, where intensity of the 50 rod CTR scattering is modulated by the excitation of the 004 Bragg reflection. It was shown that the modulation profile can be characterized by two parameters: the phase shift, which represents the dip or peak position of the modulation profile, and the visibility. The solid (red) line in Fig. 1 is the best-fit curve calculated, where the phase shift and visibility are fixed at $-2\pi\times(0.117 \pm 0.001)$ and 0.521 ± 0.002. Both the experimentally obtained values were different from those of an ideal perfect crystal (0 and 0.711, respectively), which is shown by the dotted line in the figure.

Figure 2 shows an illustration of the strain field under the SiO_2/Si(001) interface which can explain the experimen-

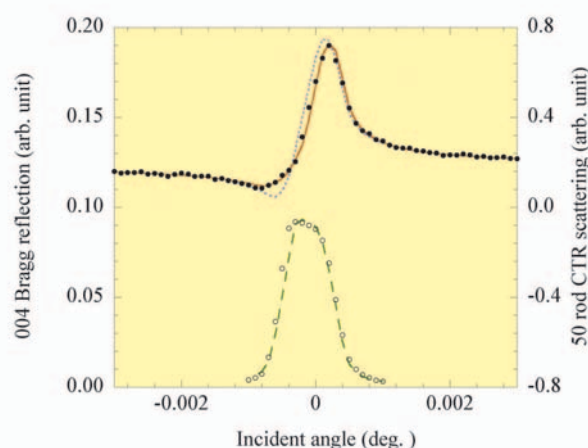

Fig. 1. Intensity of the CTR scattering is modulated by the excitation of a Bragg reflection [1,2]. An example is demonstrated in the case of a Si(001) wafer covered with a thermal oxide layer. The experiment was carried out at BL09XU in SPring-8. The solid and open circles represent the experimentally obtained intensities corresponding to the 50 rod CTR scattering and 004 Bragg reflection, whose scales (in arbitrary units) are on the right and left axes, respectively. The horizontal axis is the deviation in the incident angle from the 004 Bragg angle. The dotted line is the intensity calculated for an ideal perfect crystal. The solid and broken lines are the best-fit curves to the experimentally obtained data.
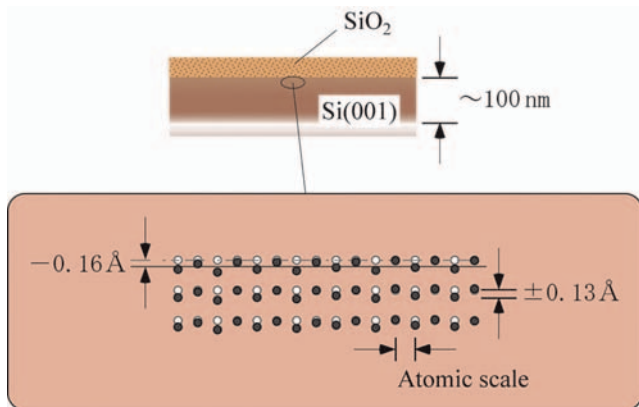
Fig. 2. Illustration of the strain field under the SiO$_2$/Si(001) interface which can explain the experimentally obtained modulation profile. The open circles represent to the cites of atoms or unit cells in bulk crystal, and the solid circles represent the position of them in the strained layer near the interface. The arrangement of the experiment was set to be particularly sensitive to strain fields distributing meso-scopic-range depth. The phase shift of modulation profile can be simply interpreted into the sum of displacements of atomic planes under the interface projected onto the direction perpendicular to the 004 plane. The phase shift in Fig. 1 shows that there is a total displacement of -0.16 Å in the direction perpendicular to the crystal surface. On the other hand the experimentally obtained visibility indicates that the total displacement has static fluctuation in the direction parallel to the interface. The visibility was interpreted into a static fluctuation of at least ± 0.13 Å in the lateral direction.

tally obtained modulation profile. The phase shift can be simply interpreted into the sum of displacements of atomic planes under the interface projected onto the direction perpendicular to the 004 plane (-0.16 Å in the figure). On the other hand the visibility indicates that the total displacement has a static fluctuation of at least ± 0.13 Å in the direction parallel to the interface. The features revealed by the PSXD technique are expected to provide a new window to understand the oxidation mechanism of Si surface.

References
[1] W. Yashiro, K. Sumitani, T. Takahashi, Y. Yoda, and K. Miki, Surf. Sci. 550 93 (2004).
[2] T. Takahashi and S. Nakatani, Surf. Sci. 326 347 (1995); W. Yashiro, K. Sumitani, Y. Yoda, and T. Takahashi, Jpn. J. Appl. Phys. 42 6658 (2003), and references therein.

Authors
W. Yashiro[a,b], K. Sumitani, Y. Yoda[c], K. Miki[a,b], and T. Takahashi
[a] Nanomaterials Laboratory (NML), National Research Institute for Materials Science (NIMS)
[b] Nanotechnology Research Institute (NRI), National Institute of Advanced Industrial Science and Technology (AIST)
[c] Japan Synchrotoron Radiation Research Institute (JASRI)

Atomically Smooth GaAs (110) Surface Fabricated by Growth-interrupt Annealing and Cleaved-edge Overgrowth

Ji-Won Oh, A. Ishii, and H. Akiyama

MBE growth of GaAs on a cleaved (110) surface is becoming of increasing importance as a fabrication method for novel semiconductor nanostructures. The overgrowth on a cleaved (110) surface requires, however, a low substrate temperature range (470 - 510°C) and a very high As$_4$-vapor overpressure for GaAs, and overgrown film has rough sur-

faces. We have found that rough as-grown (110) surface turns to an atomically smooth surface if we perform growth-interrupt in-situ annealing at 600 °C for 10 min [1]. This annealing method enables us to realize quantum wires and wells with unprecedentedly high quality.

The purpose of this joint study is to understand formation mechanisms of the atomically flat (110) GaAs surface. For this purpose, we formed annealed (110) GaAs surface with fractional monolayer (ML) coverage, and performed AFM measurements on characteristic step-edges shapes of isolated pits and islands [1], and also performed statistical analysis on the size and shape distribution of 1-ML-deep
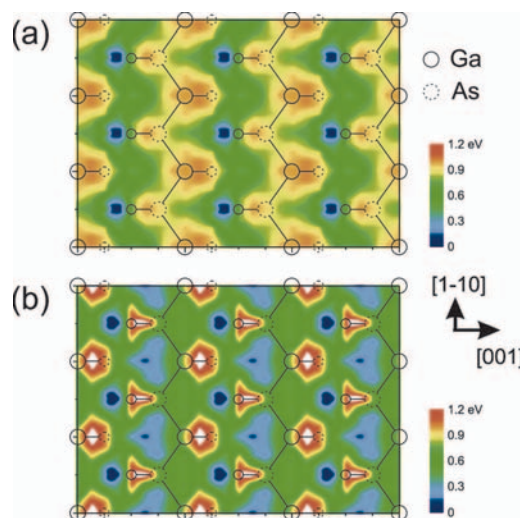

Fig1 . **(a)** Top and side views of the atomic arrangement model of a 1-ML-deep pit observed on the annealed (110) surface. This model has the Ga-terminated three-bond step-edge (A-B), the As-terminated three-bond step-edge (C-D), and the two-bond step-edges (A-D and B-C). **(b)** Atomic step kinetics of the surface evolution during annealing. Proposed schematic drawings of the evolution for the island and pit structures from an assumed square initial shape.
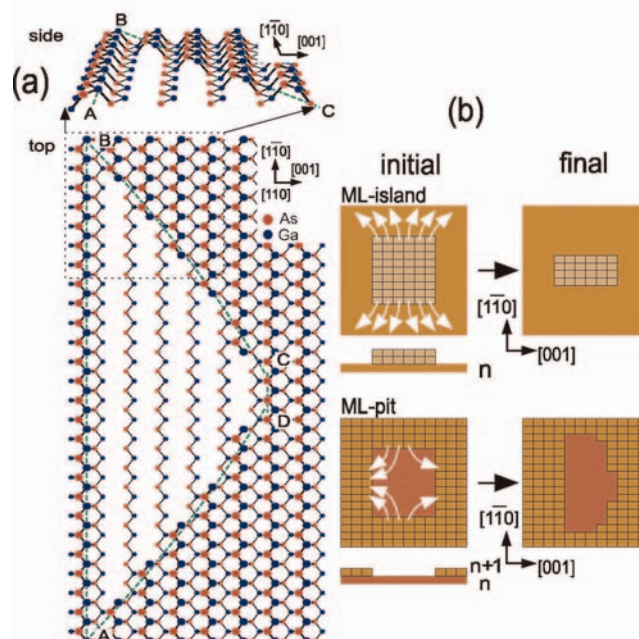

Fig. 2. Contour map of migration barrier energy for (a) Ga adatom and (b) As adatom on a GaAs (110) surface with the surface atomic configuration. The dotted and solid circles correspond to As and Ga, respectively.

pits [2].

Figure 1 shows a model for the atomic step-edges of the 1-ML-deep pit, which is based on the stability of atomic sites. Our model, namely Ga atom migration occurs from two-bond sites to three-bond sites having higher stability, well explained the driving force to form an atomically smooth surface and characteristic atomic step edges [2].

We also performed the first-principles calculation on the migration barrier energy for Ga and As adatoms on a GaAs (110) surface [3]. The results show far smaller barrier energies than those on a (100) GaAs surface, which enable adatoms to migrate in a very long length and explain the formation of a very wide atomically smooth ((110) surface as stated above.

Figure 2 (a) and (b) show the calculated potential surfaces for the Ga and As adatoms on the GaAs (110) surface. Migration barrier energy surface of Ga adatoms is 1-D, while that of As adatoms is 2-D. For both Ga and As adatoms, the stable near As of the topmost layer are very stable, while those near Ga are unstable. This fact explains the asymmetric shapes of 1 ML deep pits shown in Fig. 1 (a).

Reference
[1]M. Yoshita et al., Jpn. J. Appl. Phys. **40**, 252L (2001); Appl. Phys. Lett. **81**, 49 (2002); J. Cryst. Growth, **251** 62 (2003).
[2]J-W. Oh et al., Appl. Phys. Lett. **82**, 1709 (2003).
[3]A. Ishii et al., Appl. Phys. Lett. **83**, 4187 (2003).

Authors
Ji-Won Oh[a], A. Ishii[b], M. Yoshita, H.Akiyama, L. Pfeiffer[c], and K. West[c]
[a]JSPS foreign visiting researcher
[b]Department of Applied Mathematics and Physics, Tottori University
[c]Bell Laboratories, Lucent Technologies

ISSP Workshop

1. Superfluidity under rotation 2003 (SUR2003)

May 13, 2003

M. Kubota, H. Ishimoto

Superfluidity is being studied under rotation as often compared with the study of superconductors in various magnetic field. Actually superfluid study under rotation has a unique opportunity to study interplay between rotation and magnetic field for the p-type Fermion superfluid, liquid 3He. Another unique superfluid consists of sub-monolayer 4He film condensed on controlled porous media presents a Bose superfluid whose properties can be modified by the pore size and the film thickness over quite a wide range. One of its unique features is the possibility to reach Ω_{c2}, which is practically impossible for the case of the bulk He superfluids. The present ISSP Mini Work Shop is actually a collection of lectures by the pioneering workers and People started the activity using newly completed ISSP rotating Cryostats, Professors W.F. Vinen (Birmingham), Erkki Thuneberg (Oulu), Matti Krusius (Helsinki), Takao Mizusaki (Kyoto), Minoru Kubota(Tokyo), and John D. Reppy (Ithaca). This public ISSP Mini Work Shop(May 13-14, 2003) was followed up by continued International work shop(May 14-17), which was held by Chuzenji Lake. The information can be found at the following url:

http://www.issp.u-tokyo.ac.jp/contents/seminar/workshop/20030513-17t.html

2. Accelerators for the Super-SOR project

August 22, 2003

N. Nakamura

The Super-SOR light source is a VUV and soft X-ray third-generation synchrotron radiation source and to be operated for nationwide and worldwide users. The University of Tokyo proposed to construct it in Kashiwa Campus. The light source consists of a 1.8-GeV storage ring, booster synchrotron and pre-injector linac and top-up injection is planned to overcome a relatively short beam lifetime. The accelerators including their buildings and radiation safety system have been designed intensively for more than two years. In this workshop, the latest accelerator design and the present status of R&D on the accelerator components and subsystems were presented. The workshop was successfully completed with active discussions among the nationwide accelerator scientists and SR users of more than 40.

http://www.issp.u-tokyo.ac.jp/labs/sor/vsx/community/2003.htm

3. New findings and views on creation and destruction of coherence of lights with shorter wavelengths

November 14-15, 2003

T. Miyahara, S.Shin, and T. Suemoto

Production of coherent lights with short wavelengths has come to a new stage since plasma sources, synchrotron radiation, free electron lasers, together with conventional lasers have made a remarkable progress in the time structure, the stability, the reproducibility, as well as the spatial coherence. One of the important problems left is how to maintain the obtained coherence against various processes to cause decoherence. This problem is not easy to solve especially when the mechanism to produce the coherence could also plays a role of decoherence. In this workshop various mechanisms to create or destroy coherence were discussed with emphasis on advantages and disadvantages of various techniques to produce coherent lights. It is also confirmed that precise control of the phases of wavepackets on the material system could provide us in the future with a new method to suppress the decoherence of lights.

http://www.issp.u-tokyo.ac.jp/contents/seminar/short/20031114ws.html

4. Material researches using high-brilliance light sources

November 28-29, 2003

N. Ueno and T. Kinoshita

Recent hot results and new research possibilities using high-brilliance synchrotron radiation in materials science and technology were presented by actively working young researchers. The workshop attracted various scientists from universities, national institutes and private companies. The workshop covered wide variety of studies on nanostructures, magnetic thin films, superconducting materials, organic-device related materials, bio-related materials, surface chemistry, and molecular and atomic physics. Potential use of rather small-energy x-rays near SK edge in structural analyses of biomolecules was presented. In addition to these, actual applications of synchrotron radiation to industrial fields were introduced. Very exciting and valuable discussions were made throughout the workshop. Discussions demonstrated steady increase in scientific potential of spectromicroscopy including photoelectron emission microscopy using high-brilliance light sources.

http://www.issp.u-tokyo.ac.jp/labs/vsx/community/2003keikaku

5. Novel condensed-matter properties created by frustration

December 1-3, 2003

H. Kawamura and M. Imada

Frustration is ubiquitous in nature. It describes the situation where several optimization conditions compete with each other and are incompatible. Under frustration, the system tends to be unstable and fragile, often being subject to strong fluctuation effects. This could give rise to many interesting novel phenomena not encountered in standard unfrustrated systems.

Last year, we held an ISSP workshop "Frustrated magnetism and novel properties". Following the success of this workshop, we held this year the second one in the series, *i.e.*, "Novel condensed-matter properties created by frustration", which covered even wider areas, including, not only frustrated magnetism, but also electron transport phenomena, metal-insulator transitions, various charge and orbital phenomena closely related with frustration. Mentioning some of the specific topics hotly discussed in the workshop, magnetic ordering of kagome, spinel and pyrochlore magnets including spin and kagome ice, quantum spin ordering of geometrically frustrated magnets, chirality and its effect on transport properties such as anomalous Hall effect, nature of the ordering of spin glasses, geometrical frustration and strongly correlated electron systems including absorbed helium-three film and organic materials, superconductivity in the novel triangular-lattice oxide $Na_xCoO_2yH_2O$, etc.

http://thmat8.ess.sci.osaka-u.ac.jp/Meeting2003/

6. Frontier of surface spectroscopy and its application to nano-science

December 4-5,2003

M. Kawai and J. Yoshinobu

Recent development of surface spectroscopy in time-domain and spatial-domain enables us to investigate atoms and molecules on surfaces in detail. For instance, the dynamics including the energy tranfer and dissipation between vibrational modes and bond-fomation and bond-scission at surfaces can be observed in ps/fs time-scale using non-linear spectroscopy with pulsed laser. In the latter case, single molecular spectroscopy and manipulation on surfaces can be achieved using a local probe methods (STM, AFM, etc.). These state-of-the-art tools play an important role in nano-science and nano-technology but also gives us an opportunity to extract new concepts in physics and chemistry. Therefore the collaboration between physicist and chemists, and theoreticians and experimental researchers becomes more important. In this workshop, we presented and discussed our recent results and idea including surface vibrational spectroscopy, local-probe methods, photoelectron spectroscopy using SR and laser.

http://sas.k.u-tokyo.ac.jp/ads/

7. Superfluidity by means of vacancy excitations

December 20-21, 2003

M. Kubota

Supersolid state, which maintains the lattice order and at the same time superfluid properties, has been discussed since 1970 for the quantum solid 4He. Although various experimental search for such a state lasted for more than 30 years without any success. The general situation has been changed by recent reports by Goodkind (California) on bulk solid He and by Moses Chan (Pensilvernia) on solid He formed in porous media, especially by the latter. Namely their torsional oscillator results could derive critical velocity information. Theoretical study by Galli and Reatto predicted BEC and off diagonal long range order(ODLRO) on much more quantitative ground. ISSP mini work shop was organized to review the above situation and to present other related systems which may come into the same or similar category situation. Systems include solid He mixture near hcp- bcc phase boundary, He films condensed on glass surfaces, Hydrogen in metalhydrides. There will be new developments expected in the field. December 20-21, 2003. The information about this miniworkshop is available at the following url: http://www.nagaoka-ct.ac.jp/mb/lab/araki/issp-tanki2003-12/index.html

8. Frontiers in research of quantum condensed systems

January 7-9, 2004

K. Shirahama, H. Ishimoto, and M. Kubota

Condensed helium is unique in condensed matter physics: it shows a large variety of quantum phenomena at low temperatures. Since similar phenomena have been observed in other systems such as alkali Bose gases and heavy fermion superconductors, liquid and solid helium draw renewed interests as counterpart and model systems. Moreover, recent contributions from Japanese groups have been of great importance in the research fields. We organized this three-day workshop to serve as a forum for discussing recent outcome, common problems and concepts in helium and various research fields. We have made fruitful discussions on the following topics: anisotropic superfluids and superconductors, low dimensional ^{3}He and quantum spin systems, helium in restricted geometries, surface and interface phenomena, quantized vortices and Bose condensation. A series of workshops are planned including the ninth ISSP International Symposium (ISSP-9) on Quantum Condensed System, held at 16 - 19 November, 2004 (http://www.issp.u-tokyo.ac.jp/issp-9/).
http://www.phys.keio.ac.jp/labs/sirahama/2004_ISSP-tanki/ sirahama-jp.html

9. High pressure material seminar21: Pressure induced quantum critical phase transitions

February 5-6, 2004

Y. Uwatoko

In recent years, many researchers do investigate a study to high pressure science. The seminar is focused on the high pressure science and technology. To cover the entire diversity in methodology, experimental techniques, application, and theory of high pressure science and technology, the scientific program is organized in lectures and poster sessions. In addition to the scientific program, the progress and development of new pressure techniques are an important part of the workshop. Special emphasis are put on the needs of the high pressure user community, future developments and new perspectives.
http://www.issp.u-tokyo.ac.jp/labs/extreme/uwatoko/tanki_top.html

10. Recent progress in ultrafast laser spectroscopy

February 16-17, 2004

T. Suemoto

Ultrafast laser spectroscopy has become a matured technology owing to the titanium sapphire lasers with a very high performance and stability developed in the 1990s.

In addition to the lasers in the near infrared and visible regions, coherent light sources in the vacuum ultraviolet and the terahertz frequency regions are being developed in recent days. This workshop focused on these new light sources, spectroscopic methods utilizing the properties of these advanced lasers, and their applications to material science. It was also intended to overview the activities of this field in Japan before the 16th International Conference on Ultrafast Phenomena, which will be held at Niigata in July. Twenty-three oral presentations involved topics on non-linear phenomena, photoelectron spectroscopy, wave-packet dynamics, photo-induced phase transitions, terahertz radiation and so on. Dynamical studies on a wide range of materials, i.e., semiconductors, nano-structures, strongly correlated systems, organic crystals and biomaterials were covered in the workshop.
http://www.issp.u-tokyo.ac.jp/contents/seminar/short/tanki20040216.html